American Mineralogist, Volume 76, pages 370–396, 1991

Alpha-decay damage in titanite

FRANK C. HAWTHORNE, LEE A. GROAT,* MATI RAUDSEPP,
NEIL A. BALL, MITSUYOSHI KIMATA,**
FELIX D. SPIKE, ROBERT GABA,† NORMAN M. HALDEN
Department of Geological Sciences, University of Manitoba, Winnipeg, Manitoba R3T 2N2, Canada

GREGORY R. LUMPKIN,‡ RODNEY C. EWING
Department of Geology, University of New Mexico, Albuquerque, New Mexico 87131, U.S.A.

ROBERT B. GREEGOR, F. W. LYTLE
The Boeing Company, Seattle, Washington 98124, U.S.A.

T. SCOTT ERCIT
Division of Mineral Sciences, National Museum of Natural Sciences, Ottawa, Ontario K1A 0M8, Canada

GEORGE R. ROSSMAN
Division of Geological Sciences, California Institute of Technology, Pasadena, California 91125, U.S.A.

FREDERICK J. WICKS, ROBERT A. RAMIK
Department of Mineralogy, Royal Ontario Museum, 100 Queen's Park, Toronto, Ontario M5S 2C6, Canada

BARBARA L. SHERRIFF,§ MICHAEL E. FLEET
Department of Geology, University of Western Ontario, London, Ontario N6A 5B7, Canada

CATHERINE MCCAMMON‖
Department of Geological Sciences, University of British Columbia, Vancouver, British Columbia V6T 2B4, Canada

ABSTRACT

Titanite can incorporate minor amounts of radioactive impurity components (particularly U and Th) that affect the crystal structure by α- and β-decay events; in particular, α-decay gives rise to significant knock-on structural damage by causing atomic displacements. We have examined a series of chemically and structurally well-characterized titanite samples by a variety of techniques to follow the progress of the metamictization process at low radiation doses. Ten titanite samples were characterized by electron microprobe analysis, powder X-ray diffraction, and powder infrared (IR) spectroscopy. The X-ray diffraction patterns vary from sharp and well resolved to almost totally degraded, reflecting the various degrees of α-decay damage. The powder IR spectra show a similar variation, and the order of increasing pattern degradation is almost the same as that for the X-ray diffraction patterns, indicating that both features reflect the same physical property of the material. However, the annealing behavior is different: powder X-ray diffraction patterns become sharp and well resolved; powder IR spectra sharpen slightly, but do not recover to anywhere near the same extent.

Four representative samples were selected for further work. The crystal structures were refined using Mo$K\alpha$ X-ray single-crystal diffraction data. The crystals were then annealed at 1090 °C under Ar and the intensity data were again measured. For small degrees of α-decay damage, the structure seems to be completely restored on annealing; this is not the case for titanite with the largest amount of α-decay damage. Polarized single-crystal IR spectra of undamaged titanite show a single sharp (OH) stretching band at ~3490 cm^{-1} with a little fine structure reflecting local cation disorder around the OH. With increasing

* Present address: Department of Geological Sciences, University of British Columbia, Vancouver, British Columbia V6T 2B4, Canada.

** Present address: Institute of Geosciences, University of Tsukuba, Ibaraki 305, Japan.

† Present address: Manitoba Department of Energy and Mines: Geological Services, Eaton Place, Winnipeg, Manitoba R3C 4E3, Canada.

‡ Present address: Australian Nuclear Science and Technology Organization, Advanced Materials Division, Menai NSW 2234, Australia.

§ Present address: Department of Geological Sciences, University of Manitoba, Winnipeg, Manitoba R3T 2N2, Canada.

‖ Present address: Bayerisches Geoinstitut, Universität Bayreuth, Postfach 101251, 8580 Bayreuth, Germany.

0003–004X/91/0304–0370$02.00

α-decay damage, the sharpness of the absorption band decreases and a wide wing appears on the low-energy side of the sharp (OH) band. Mössbauer spectroscopy shows only Fe^{3+} to be present in undamaged titanite; as α-decay damage increases, the amount of Fe^{2+} increases, suggesting that radioactive decay causes reduction as well as atomic displacement. Fe^{2+} is easily oxidized on heating. The ^{29}Si MAS-NMR peak width is strongly correlated with increasing radiation damage and increasing Fe content, and no signal was observed from the most damaged titanite. With increasing α-decay damage, single-crystal electron diffraction patterns develop diffuse halos indicative of a mean atomic spacing of 3.6 Å. In bright field, undamaged material shows continuous lattice fringes. Small amounts of damage are characterized by mottled diffraction contrast superimposed on largely continuous lattice fringes. The most damaged titanite shows mottled diffraction contrast with coexisting crystalline and aperiodic domains produced by overlapping α-recoil tracks, corresponding to damage on the order of 30–50% of that required to render the structure fully aperiodic. Ti XANES spectra show intensification of the principal pre-edge feature ($1s \rightarrow 3d$ transition) with increasing damage, indicative of increasing local asymmetry around the Ti position. Loss of resolution in the EXAFS spectra also indicates increasing disorder around Ti with increasing damage. There is no sign of any $^{[4]}Ti$ in even the most damaged samples, although it was detected in a glass of titanite composition. The metamictization process begins by the formation of isolated α-recoil and α-particle tracks. With increasing dose, the α-tracks begin to overlap, producing aperiodic domains; in the most damaged titanite examined, there were approximately equal amounts of coexisting crystalline and aperiodic material. At this stage, the crystalline domains still retain their original orientation, except where affected by low-temperature annealing. As undamaged titanite does not (usually) contain significant Fe^{2+}, it seems that the damage process is accompanied by reduction of $Fe^{3+} \rightarrow Fe^{2+}$, which resides in the aperiodic domains. These domains incorporate much more hydrogen (as OH) than is contained in crystalline titanite, presumably a result of postdamage diffusion of H into the structure.

All information is consistent with the Ewing model for metamict materials, an aperiodic random network structure; HRTEM images show patterns of random contrast consistent with the random network model, with no evidence to support any microcrystalline model of the metamict state. High-temperature annealing only partly restores the structure, the apparent degree of recovery being dependent on the coherence length of the experimental technique used to characterize the material. The degree of recovery is also dependent on the amount and pattern of damage. We suggest that the original structure is recovered when the ratio of surface area to volume for the damaged material is high, and the interface can exert a strong memory effect on the amorphous material; when large equant aperiodic domains form, they are annealed to a more defect-free and relatively stable aperiodic network structure.

Introduction

Titanite is a common accessory mineral in igneous and metamorphic rocks. The ideal formula may be written as $CaTi(SiO_4)O$, but there can be extensive substitution at both cation and anion sites within the structure. Most common are substitutions at the octahedrally coordinated Ti site; Al (Hollabaugh and Foit, 1984), Fe^{3+} (Muir et al., 1984), Ta (Groat et al., 1985), and Nb (Paul et al., 1981) can collectively substitute for up to approximately 30 mol% (Higgins and Ribbe, 1976) of that site. It is often assumed that only Si occupies the tetrahedrally coordinated site, but Hollabaugh and Rosenburg (1983) have shown that this is not necessarily the case; even in synthetic titanite, small amounts of Ti can replace Si at the tetrahedral site. At the seven-coordinate site, Ca may be replaced by what is usually minor amounts of Na, REEs, Y, U, and Th. Most of these substitutions involve heterovalent cations, and they generally couple in some fashion to maintain overall electroneutrality. However, this constraint also results in substitutions at the site of the (O) anion that is not bonded to Si. Thus $(OH)^-$ and F^- can replace O^{2-} in significant amounts, coupling with the cation substitutions to satisfy the overall constraint of electroneutrality.

The structure of titanite was solved by Zachariasen (1930) and refined by Mongiorgi and Riva de Sanseverino (1968), both studies assigning the space group $C2/c$ (or a symmetrical equivalent) to the structure. Here we use the conventional C-centered orientation throughout, so that titanite has the same orientation as related structures (e.g., minerals of the kieserite group, Hawthorne et al., 1987, and the amblygonite-montebrasite group, Groat et al., 1990). Robbins (1968) showed that synthetic $CaTi(SiO_4)O$ has the space group $P2_1/c$, and Speer and Gibbs (1976) refined the structure of the synthetic material, proposing a domain structure. Taylor and Brown (1976) refined the structure of synthetic $CaTi(SiO_4)O$ at

various temperatures and showed that it transforms to a *C*-centered (*C*2/*c*) structure at 220 °C. With increasing substitution, the structure becomes *C* centered at room temperature (Higgins and Ribbe, 1976). The structure of an Al-rich titanite was refined by Hollabaugh and Foit (1984), who showed that in the centered space group, the maximum displacement of most atoms is subparallel (to [001] in our orientation), presumably reflecting positional disorder due to incipient development of a domain structure.

Radiation damage in titanite

Natural titanite can contain significant amounts (up to ~0.2 wt%) of radionuclides, specifically U and Th, together with their daughter products in the ^{238}U, ^{235}U, and ^{232}Th decay series. The end products of these decay series are the isotopes of Pb produced by α-, β-, and γ-decay events. All three decay events cause ionization, but α-decay also gives rise to significant knock-on structural damage by causing atomic displacements. Two separate simultaneous processes are associated with the α-decay event: (1) a 4.5 MeV α-particle is emitted with a range of $\sim 10^4$ nm; most of its energy is dissipated by ionization, but at the end of its track it displaces several hundred atoms, forming Frenkel defects; (2) the parent nucleus recoils (energy ~0.07 MeV) with a range of ~10 nm, producing several thousand atomic displacements and forming tracks of disordered material. The end product of the decay process is considerable structural damage, resulting in an aperiodic structure, the metamict state (Ewing et al., 1987).

There has been significant recent interest in the metamict state and the amorphization process in natural minerals, fueled by the need to evaluate the long-term durability of ceramic nuclear waste forms that will be actinide hosts (Lutze and Ewing, 1988). Work has focused on zircon, titanite, and the pyrochlore-group minerals (Chakoumakos et al., 1987; Fleet and Henderson, 1985; Lumpkin and Ewing, 1988). The Canadian Nuclear Fuel Waste Management program has been interested in the possibility of waste storage with glass ceramics containing crystalline titanite embedded in an aluminosilicate glass (Hayward and Cecchetto, 1981; Hayward, 1988). This has promoted considerable work on radiation damage in both natural and synthetic titanite using a variety of techniques, including powder X-ray diffraction, DTA, infrared spectroscopy (Vance and Metson, 1985), crystal structure refinement (Fleet and Henderson, 1985), and Mössbauer spectroscopy (Muir et al., 1984). In addition, there has been some work on the leaching characteristics of both natural and synthetic titanite (Bancroft et al., 1987). The work reported here developed from a student project started nine years ago and grew (and grew) into an effort to characterize (by a wide variety of techniques) radiation damage in a coherent suite of titanite samples exposed to a range of radiation doses and to understand the mechanism of metamictization in titanite.

Experimental

Samples were obtained from the collection at the Department of Mineralogy, Royal Ontario Museum, Toronto, Ontario. Sample numbers and localities are given in Table 1. Densities of samples selected for further work were determined using Clerici solution and a pycnometer of known volume. Some comment on the sample M28696 from Cardiff is necessary. Titanite from this locality is very different from sample to sample. We selected material that was black and glassy in appearance but also noted the occurrence of brownish titanite from the same locality. The latter was examined by Fleet and Henderson (1985). Comparison of the electron microprobe analyses of each material showed significant compositional differences among them, as well as differences in physical appearance.

Microprobe analyses

Analyses were done on a JEOL 733 microprobe with Tracor Northern 5500 and 5600 automation. The operating potential was 15 kV with a beam current of 25 nA. The beam diameter was set at 10 μm as a safeguard against potential sample damage during electron bombardment. Data for standards were obtained for 25 s or the time corresponding to 0.25% precision, whichever was attained first. The standards used were titanite (Ca$K\alpha$, Ti$K\alpha$, Si$K\alpha$), almandine (Fe$K\alpha$, Mg$K\alpha$, Al$K\alpha$), a REE-bearing silicate glass (REE$L\alpha$, Y$L\alpha$),synthetic manganocolumbite (Mn$K\alpha$, Nb$L\alpha$), $NiTa_2O_6$ (Ta$M\alpha$), sodic amphibole (Na$K\alpha$), topaz (F$K\alpha$), ThO_2 glass (Th$M\alpha$), UO_2 glass (U$M\alpha$), zircon (Zr$L\alpha$), apatite (P$K\alpha$), and cassiterite (Sn$L\alpha$). No other elements were observed in energy-dispersive spectra obtained from the grains. Data for the REEs were corrected for line overlaps prior to reduction. Data reduction was done with a conventional ZAF routine in the Tracor Northern Task series of programs. For all analyses, peak heights were used as estimates of peak intensity (area), except in the case of F, for which a correction factor was applied to the peak height to convert it to peak intensity.

Where possible, two analyses were obtained on fresh regions of each grain: center and edge analyses for large grains and on separate grains for fine-grained samples. In addition, altered regions of samples showing evidence (in backscattered electron images) of postmetamictization alteration were analyzed. For the purposes of formula recalculation, all Fe was assumed to be trivalent, except where Mössbauer spectra indicate that Fe is present in both valence states. The formulae were calculated on the basis of 4(Si + P) per unit cell (Higgins and Ribbe, 1976). OH was calculated for charge balance assuming 20 anions; as this calculation ignores adsorbed or absorbed H_2O in structurally damaged regions, the H_2O given (Table 2[1])

[1] Copies of Tables 2 and 8 may be ordered as Document AM-91-455 from the Business Office, Mineralogical Society of America, 1130 Seventeenth Street NW, Suite 330, Washington, DC 20036, U.S.A. Please remit $5.00 in advance for the microfiche.

TABLE 1. Provenance and miscellaneous information for titanite samples

X-ray D.I.*	IR D.I.	U (ppm)	Th (ppm)	Density g/cm³	Catalog number (ROM)	Locality
1	1	—**	—	—	UK-1	Unknown
2	2	—	—	—	M6535	St. Gotthard, Switzerland
3	3	22	1	3.531	M28658	Maevatanana, Malagasy Republic
4	5	—	—	3.545	M22995	Kola, U.S.S.R.
5	4	—	—	—	E2311	Binn, Switzerland
6	7	173	450	3.563	E2312	Sebastapol Twp., Ontario
7	6	—	—	—	E3394	Henderson Co., N. Carolina
8	9	2620	100	3.567	M28173	Gjerstad, Norway
9	8	—	—	3.568	E2335	Arendal, Norway
10	10	797	470	3.461	M28696	Cardiff U Mine, Ontario

* D.I. is the damage index; the numbers 1–10 denote increasing structural damage (decreasing crystallinity as estimated from decreasing peak resolution in powder X-ray diffraction patterns (Fig. 4) and powder infrared spectra (Fig. 9).
** — = Not determined.

should be considered as a minimum estimate. In addition, for the samples on which the extensive work was done, Th and U were analyzed by neutron activation.

Thermogravimetric and evolved gas analyses

A Mettler TA-1 thermoanalyzer equipped with an Infinicon IQ200 quadrupole mass spectrometer was used to obtain the TG-EGA data. Fragments were lightly ground in an agate mortar under HPLC-grade methanol; the finest suspended fraction was rejected to reduce sample surface area and thereby minimize possible effects due to surface adsorption. Air-dried samples were weighed directly in vacuum-baked Pt crucibles and left in vacuo at near-ambient temperatures until the system reached 10^{-7} torr (1–2 h). The samples were then heated at 10 °C/min in vacuo to at least 1325 °C, cooled in vacuo, and reweighed. The same procedure was applied to a 30-mg α-alumina sample to provide EG curve baselines. H_2O is the most abundant residual gas in the system. Consequently the sensitivity to evolved H_2O is lower than for other volatiles. For example, the sensitivity to evolved H_2 is at least an order of magnitude higher.

Annealing

Samples were annealed at 1090 °C for 3.7 h in open $Ag_{60}Pd_{40}$ capsules under an Ar atmosphere. Sample E2312 did not change color, M28173 changed from light tan to gray, Cardiff changed from light gray to darker gray, and M28658 changed from pale green to amber.

X-ray powder diffraction

Powdered samples were prepared by breaking the material with a hammer to a maximum fragment size of 1–2 mm; a magnet was then used to remove any metal introduced at this stage. The fragments were ground by hand under methanol in an alumina mortar and dried under a heat lamp. The resulting powder was sieved through a 200-mesh nylon screen. X-ray powder diffraction patterns were recorded on a Philips PW1710 automated powder diffractometer using Ni-filtered Cu$K\alpha$ radiation and a scan speed of 0.3° 2θ/min.

Infrared spectroscopy

High-resolution infrared spectra of powdered titanite in the region 4000–400 cm^{-1} were recorded on a Nicolet Fourier-transform infrared spectrophotometer, Model MX-1, equipped with a Nicolet 1280 computer for signal processing. The sample chamber was purged with dry N_2 before and during spectrum collection. Frequency measurements were calibrated internally against a He-Ne laser and are accurate to 0.01 cm^{-1} according to the manufacturer.

Powdered samples were prepared by grinding 200 mg of titanite by hand in an alumina mortar. The powder was agitated in a vial of ethanol and allowed to settle for 1 h. Stoke's law was used to calculate the depth to which a 2-μm titanite grain would settle in this time, and a suspension at this depth was withdrawn by pipette; the resulting powder has an average grain size of 2 μm. A 0.5-mg sample was mixed with 210 mg of sieved (<400 mesh) and dried (at 200 °C) KBr in a dentist's amalgamator (Wig-L-Bug); it was then pressed in an evacuated, heated die into a 13-mm pellet that was stored in a dessicator prior to use.

For the single-crystal spectra, a large crystal was aligned on a precession camera. The goniometer head was then removed from the camera and mounted on a spindle stage. From here, the crystal was sunk into a rectangular perspex box filled with liquid 5-minute epoxy. Upon solidification, the block was sawed into slices in the appropriate orientations for polarized infrared spectroscopy. The slices were glued to frosted glass slides, ground to a thickness of ~100 μm, polished on both sides, and removed from the supporting glass sections. Spectra were recorded at 23 °C on a Nicolet 60SX FTIR spectrometer equipped with a $LiIO_3$ polarizer. The spectra were taken through a 600-μm diameter brass aperture that was positioned to avoid cracks and visible inclusions.

Single-crystal X-ray diffraction

Equant single crystals of selected samples of titanite were mounted on glass fibers and aligned on a precession camera using Mo$K\alpha$ X-radiation. Zero-level precession

TABLE 3. Cell dimensions for natural (unannealed) titanite

	a (Å)	b (Å)	c (Å)	β (°)	V (Å^3)
M6535	6.551(1)	8.700(2)	7.057(2)	113.88(2)	367.9(1)
M28658	6.549(1)	8.695(1)	7.060(1)	113.87(1)	367.6(1)
M22995	6.562(1)	8.715(2)	7.071(2)	113.89(2)	369.7(1)
E2311	6.553(1)	8.700(1)	7.063(1)	113.90(1)	368.1(1)
E2312	6.562(1)	8.715(2)	7.076(1)	113.94(2)	369.8(1)
E3394	6.559(1)	8.718(2)	7.073(2)	113.87(2)	369.8(2)
M28173	6.564(1)	8.719(1)	7.057(1)	113.79(1)	369.5(1)
E2335	6.580(2)	8.750(2)	7.058(2)	113.77(2)	371.9(2)
Cardiff	6.603(2)	8.766(2)	7.099(3)	114.01(2)	375.3(2)

photographs were recorded using short exposures; no reflections violating C centering were seen on these photographs.

Crystals of all samples were ground into spheres or ellipsoids to minimize differential absorption as a function of orientation and mounted on a Nicolet R3M automated 4-circle diffractometer. Twenty-five reflections were centered using graphite-monochromated Mo$K\alpha$ X-radiation. Least-squares refinement of the setting angles produced the cell dimensions listed in Table 3 and the orientation matrix relating the crystal axes to the diffractometer axes. Intensity data were obtained in the θ-2θ scan mode with scan rate dependent on peak intensity. The backgrounds were measured at the beginning and end of each scan. Two standard reflections were monitored every 48 intensity measurements to check for stability and alignment; no significant variations were noted. Reflections were measured over one asymmetric unit to a maximum 2θ of 60° for a primitive unit cell. Ten strong reflections uniformly distributed with regard to 2θ were measured at 10° intervals of ψ (the azimuthal angle corresponding to rotation of the crystal about its diffraction vector) from 0 to 350°. These data were used to calculate an ellipsoidal absorption correction that was then applied to the entire data set. Data were corrected for Lorentz, polarization, and background effects, and reduced to structure factors; reflections were classed as observed if their intensity exceeded that of four standard deviations based on counting statistics. Data measurement and refinement information are summarized in Table 4. For sample M28658, previously judged the most crystalline, only six primitive reflection intensities ($h + k = 2n + 1$) were observed, and none exceeded five standard deviations (based on counting statistics). In addition, efforts to refine the M28658 structure in $P2_1/c$ were not successful. Consequently, the C-centered space group was used. After satisfactory refinement of the structures of these crystals, they were annealed, the data measurement repeated, and the structures refined again.

Mössbauer spectroscopy

Powdered samples were mixed with benzophenone to ensure random orientation of the grains; the amount of sample used was chosen such that the amount of Fe was ~5 mg/cm^2. Spectra were obtained at room temperature using a constant acceleration Mössbauer spectrometer and stored in a 512-channel analyzer until ~2×10^6 off-resonance counts per channel had accumulated. Velocity calibration was done using metallic Fe foil, and the Mössbauer parameters are given relative to this standard at room temperature.

Magic-angle spinning NMR

The ^{29}Si MAS-NMR spectra were recorded at a frequency of 99.36 MHz with a spectral width of 50000 Hz on a Bruker AM-500 Fourier-transform spectrometer. The samples were spun at approximately 3500 kHz at an angle of 54.7° to the magnetic field using a magic-angle-spinning probe (Fyfe et al., 1982). Delays between pulses varied between 5 s for the low-Fe sample and 0.1 s for the high-Fe sample. The line broadening applied during Fourier transformation to reduce background noise was dependent on signal strength and resolution, with 100 Hz applied for the high-Fe samples, 50 Hz for sample M28658, and 10 Hz for the synthetic titanite. Chemical shifts were measured in ppm with reference to tetramethylsilane.

High-resolution transmission electron microscopy

Powdered aliquots of samples M28658, M28173, and Cardiff were dispersed in acetone and deposited on Cu grids covered with holey carbon film. Samples were examined using a JEOL 2000FX transmission electron microscope operating at 200 kV. Low-resolution bright-field images were recorded at a magnification of 100000. HRTEM phase-contrast images were recorded at a magnification of 410000 using axial illumination with the objective lens defocused by −650 to −1000 Å.

A Tracor Northern TN-5500 energy-dispersive X-ray analysis system was used to monitor the compositions of the three samples. EDS spectra were acquired for 200 s of live time (system dead time was 15–20%) using an effective beam size of 10 nm. Data reduction was done with a standardless metallurgical thin-film technique (SMTF, Tracor Northern software) with k factors derived from silicate reference samples.

EXAFS and XANES spectroscopy

The EXAFS-XANES experiments were done at the Stanford Synchrotron Radiation Laboratory (SSRL). At SSRL, the side station of wiggler Beam Line IV-1 was used with the synchrotron beam at a current of approximately 30–60 mA and an energy of 3 GeV. A Si(220) double-crystal monochromator was used for the TiK edges, with the angle between the crystal faces detuned such that the diffracted beam intensity was reduced by 50% to reduce the harmonic content of the beam. The monochromator was moved in 0.25-eV steps in the vicinity of the K edge, which was approximately the resolution of the system at the TiK edge. The data were obtained at room temperature using powdered samples (200 mesh)

contained in 0.25-mil polypropylene bags using a fluorescent X-ray detector (Stern and Heald, 1979; Lytle et al., 1984). Self-absorption in the fluorescent mode was assumed to be minimal, as we have observed minimal self-absorption in fluorescent data for other Ti samples (pyrochlore and $SrTiO_3$) by comparing fluorescent yield, e yield, and absorption; also, the fluorescent data were of better quality than the absorption data. A complete description of the techniques used to analyze the data is given in Greegor et al. (1984).

Results

Chemistry

The electron microprobe analyses and unit formulae are given in Table 2. The cation sums for the Ca and Ti sites were calculated assuming all Ca, Na, Mg, Mn, REE, Y, Zr, U, and Th to be at the Ca site, and all Ti, Fe^{3+}, Al, Sn, Nb, and Ta to be at the Ti site. The results are shown in Figure 1; the mean site sums are within 0.5% of the ideal value of four cations per unit cell, attesting both to the validity of the formula calculation scheme and to the absence of significant ZAF calculation errors. The cation sums at each site are normally distributed with no evidence of significant skewness, supporting the site assignments given.

Higgins and Ribbe (1976) noted the relationship between Al + Fe and OH + F in titanite. Figure 2 shows the well-developed positive correlation between these two variables, with an intercept of zero and a slope close to unity, supporting the substitution $(Al,Fe^{3+}) + (OH,F)^- \rightleftharpoons Ti^{4+} + O^{2-}$ as the dominant mechanism for introducing monovalent anions into the structure. Previous work (e.g., Paul et al., 1981; Groat et al., 1985) has shown that the mechanism $(Al,Fe^{3+}) + (Nb,Ta) \rightleftharpoons 2\ Ti^{4+}$ is primarily responsible for the incorporation of pentavalent cations into the titanite structure; however, as is apparent from Figure 2, there is not enough (Al,Fe^{3+}) in the titanite samples of the present study to account for all (OH,F) present, much less additional minor (Ta,Nb). All titanite samples examined were REE bearing, with (Y + REE) ranging from 0.01 to 0.13 cations per unit cell.

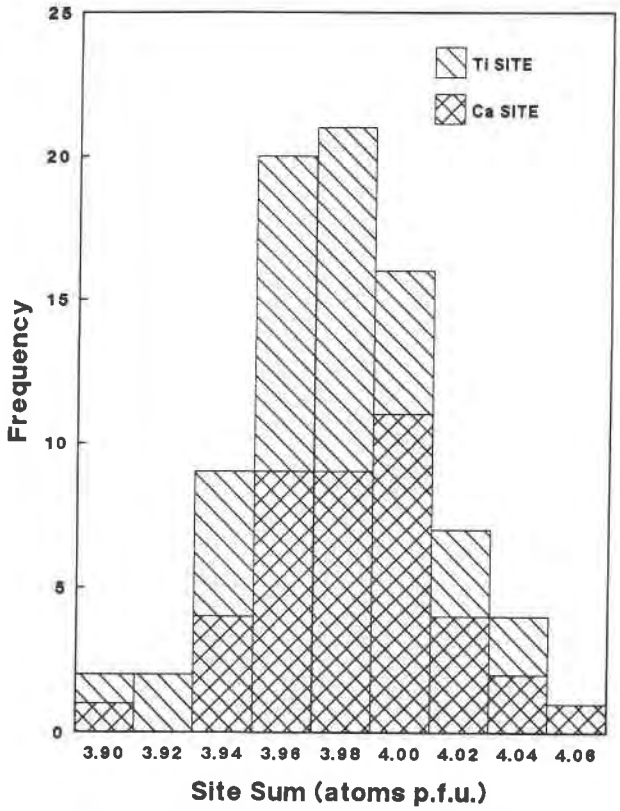

Fig. 1. Histograms of cation site sums (per 20 anions) for the analyses given in Table 2.

Associated phases are listed in Table 5. As expected, contents of minor elements generally correspond to the type of associated minerals: E3394 is the only sample that has abundant zircon inclusions, and it has the highest Zr content; titanite without uraninite or thorite inclusions does not have U or Th that is detectable using the elec-

Table 4. Structure refinement data for selected natural and heated titanite samples

	M28658		E2312		M28173		Cardiff	
	Natural	Heated	Natural	Heated	Natural	Heated	Natural	Heated
a (Å)	6.549(1)	6.539(1)	6.554(1)	6.547(1)	6.564(1)	6.538(1)	6.607(2)	6.530(2)
b (Å)	8.695(1)	8.692(1)	8.708(1)	8.695(2)	8.719(1)	8.699(1)	8.775(3)	8.677(2)
c (Å)	7.060(1)	7.037(1)	7.069(1)	7.059(1)	7.057(1)	7.044(1)	7.110(3)	7.048(2)
β (°)	113.87(1)	113.79(1)	113.93(1)	113.94(1)	113.79(1)	113.76(1)	114.08(3)	113.91(2)
V (Å^3)	367.6(1)	366.0(1)	368.8(1)	367.3(1)	369.5(1)	366.6(1)	376.3(2)	365.1(1)
Space group	$C2/c$	$C2/c$	$C2/c$	$C2/c$	$C2/c$	$C2/c$	$C2/c$	$C2/c$
Size (mm)	0.12 × 0.12 × 0.14		0.14 × 0.18 × 0.20		0.10 × 0.12 × 0.14		0.10 × 0.14 × 0.16	
Rad/Mon	Mo/Gr	Mo/Gr	Mo/Gr	Mo/Gr	Mo/Gr	Mo/Gr	Mo/Gr	Mo/Gr
No. of I	1278	637	1282	640	1283	639	1242	1219
No. of F	535	531	535	532	538	533	528	530
No. of F_o	492	456	484	484	465	475	459	502
R(obs)	2.6	3.3	2.1	2.5	2.9	2.7	5.7	5.5
wR(obs)	2.5	3.7	2.1	2.8	2.8	3.3	5.9	5.6

Note: $R = \Sigma(|F_o| - |F_c|)/|F_o|$; $wR = [\Sigma w(|F_o| - |F_c|)^2/\Sigma wF_o^2]^{1/2}$, $w = 1/(\sigma^2 F_o + kF_o^2)$.

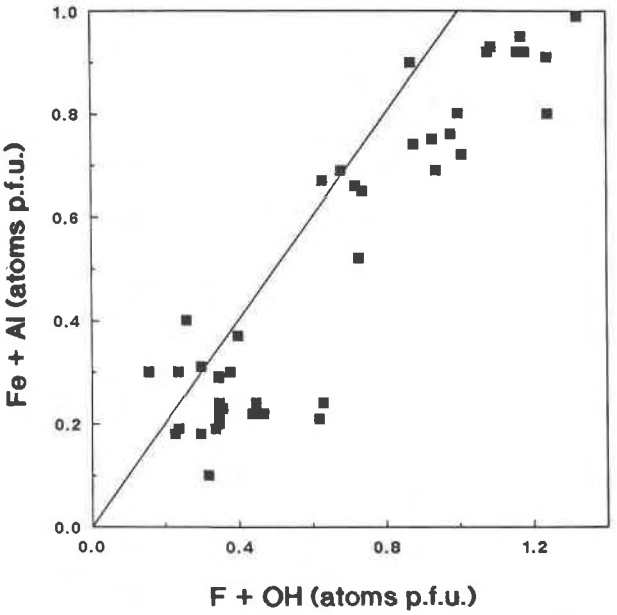

Fig. 2. Fe + Al as a function of OH + F for titanite; the line indicates (Fe + Al) : (F + OH) = 1:1 and is drawn to illustrate that these titanite samples show increasing deviation from this relationship with increasing F + OH.

tron microprobe; titanite samples with an associated (Y,REE) mineral are richest in (Y,REE); samples with fergusonite inclusions are enriched in Y relative to the REE and are enriched in Nb. Note that samples with Fe oxide or apatite inclusions are not enriched in Fe or P, respectively. Because of the presence of inclusions in the separates analyzed for U and Th, the values given in Table 1 must be considered as upper estimates.

The X-ray diffraction and infrared spectroscopy results showed the sample from Cardiff to be significantly damaged. Heating experiments (see the experimental section) were done to attempt to anneal and restore crystallinity. The electron microprobe analyses show that heating has little or no effect on the chemical composition of the metamict samples. This contrasts with natural postmetamictization alteration, which can be seen in the Cardiff samples in backscattered electron images. Backscattered electron images of the natural metamict samples show two regions of significantly different chemical composition. Altered or replaced regions occur along fractures, suggesting that these regions have been altered or recrystallized by secondary fluids that have invaded the titanite along the fractures. These regions are generally closer to the ideal formula $CaTiSiO_5$ than the regions away from the fractures; all cation sites have occupancies closer to those of the end-member formula.

TABLE 5. Minerals associated with the titanite samples of Table 2

Sample	Associated minerals
M6535	zircon
M22995	apatite, fersmanite, ferro-richterite
E2312(2)	synchisite-(Ce)
E3394	zircon
M28173(1)	fergusonite, uranpyrochlore, chernovite, uranophane
M28173(2)	uraninite, uranophane, fergusonite, unknown Y-Nb-Al silicate
E2335(1)	iron oxide, thorite, zircon
E2335(2)	iron oxide, allanite, synchisite-(Ce)
Cardiff(org)	allanite
Cardiff(1)	thorite, allanite, calcite, uraninite
Cardiff(2)	zircon, thorite

Thermogravimetric and evolved gas analysis

Six samples were chosen for TG-EGA such as to represent the full range of variables of interest (Table 6). The degree of crystallinity varied from high (M28658) to low (Cardiff); the F content varied from 0.27 (M28658) to 2.68 wt% (Cardiff); the Fe content varied from 0.60 wt% Fe_2O_3 (M28658) to 3.66 wt% (M28173). The Cardiff sample was the only one to contain significant Fe^{2+}; in all other samples, the Fe was present in the trivalent state.

The volatile loss at ambient temperature while pumping down to 10^{-7} torr could not be identified directly because the quadrupole mass spectrometer cannot be turned on until the vacuum is established. However, the volatile is almost certainly H_2O adsorbed on the surface of the titanite grains, and hence of little consequence here. The small losses of CO_2 identified in some analyses are probably from minor carbonate inclusions (calcite inclusions were observed in one sample) and cannot be attributed with conviction to minor substitution of $(CO_3)^{2-}$ for $(SiO_4)^{4-}$ in the titanite structure (Vance and Metson, 1985).

There was no significant loss of any volatile below ~500 °C (Table 6). In the range 500–1000 °C, H_2 and H_2O are the principal volatiles released. The samples fall into two groups:

1. Two samples (M28658 and E2335) gave H_2O with little or no H_2. In the higher temperature range (1000–1325 °C), volatile loss was either insignificant (M28658) or small (E2335); the volatiles of the latter sample condensed prior to reaching the spectrometer and could not be identified. It is notable that these two samples had only small amounts of F (Table 6), and no F-bearing species were detected at the spectrometer.

2. The remaining four samples gave H_2 as the principal species between 500 and 1000 °C, with only minor H_2O. In the high-temperature range (1000–1325 °C), these samples produced a variety of volatiles in considerable amounts, particularly SiF_4, F, HF, H_2, and O_2 (possibly with minor H_2O). These samples all have significant amounts of F (Table 6), and F-bearing species were the dominant volatiles observed at high temperatures. The relative amount of high-temperature weight loss correlates strongly with the amount of F in the titanite (Fig. 3). It is also difficult to avoid the conclusion that the presence of F in titanite is a major factor controlling the character of the evolved volatiles at lower temperatures: when F is present in significant quantities, the principal

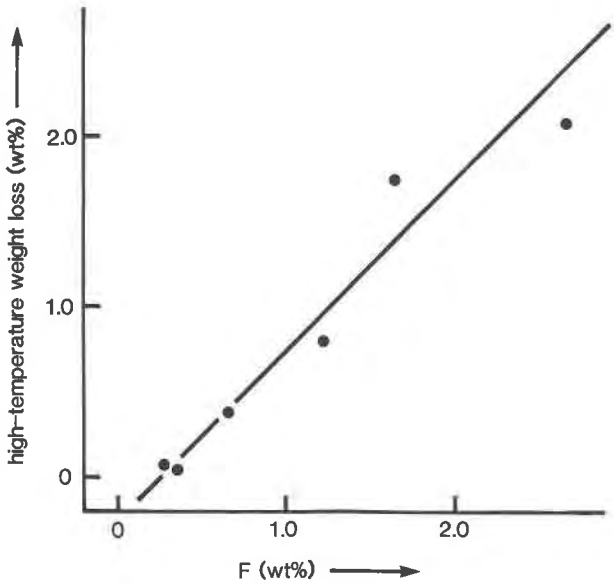

Fig. 3. High-temperature weight loss as a function of F content for selected titanite samples.

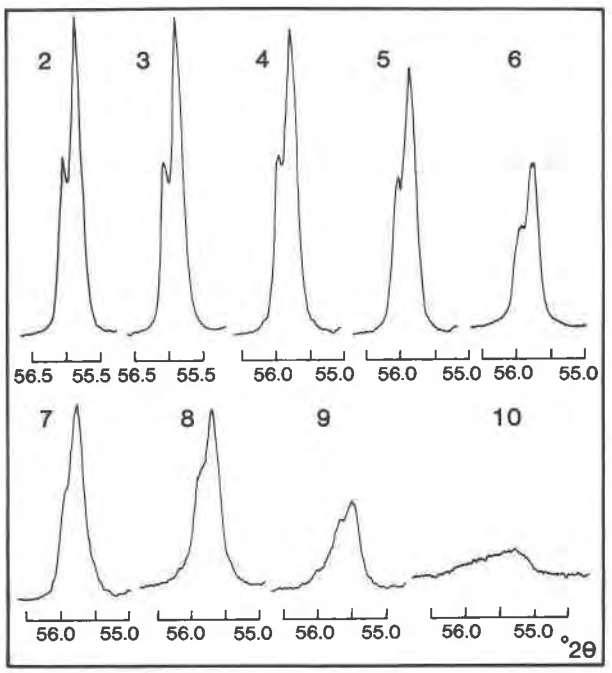

Fig. 4. The 330 X-ray diffraction peak of titanite samples in order of decreasing quality.

evolved species is H_2; however, when F is not present, the principal evolved species is H_2O.

X-ray powder diffraction

There are considerable differences in the powder diffraction patterns of the different titanite samples (Figs. 4, 5). In some patterns, the peaks are sharp and closely overlapping peaks are reasonably well resolved; in other patterns (specifically Cardiff), peaks are broad and asymmetric, with much decreased intensity, or they are absent altogether. A complete range of patterns is observed between these two end-members; the samples were ranked by degree of pattern degradation as estimated by eye and assigned a number, designated as the damage index (see Table 1). Of particular use in this procedure is the (330) peak at ~56° 2θ. Figure 4 shows this peak (with the α_1-α_2 doublet resolved) for the samples listed in Table 1. For equal weights of sample, there is a gradual degradation of peak sharpness and intensity that was taken as indicative of increasing degree of α-decay damage. The samples M28658, E2312, M28173, and Cardiff were selected as typical examples of gradually increasing X-ray diffrac-

Table 6. Thermogravimetric and evolved gas analyses of selected titanite samples

Sample number	Weight (mg)	Temperature range (°C)	Weight loss (wt%)	Volatiles	F (wt%)	Fe_2O_3 (wt%)	Damage index
M28658	23.537	ambient	0.04	n.a.	0.27	0.60	3
		510–995	0.17	H_2O [CO_2]			
		1100–1325	0.04	[O_2?]			
M22995	51.823	ambient	0.02	n.a.	0.64	1.35	4
		150–900	0.03	[H_2, H_2O?]			
		900–1360	0.38	O_2, HF [CO_2, H_2O?]			
E2312	14.39	ambient	0.00	n.a.	1.64	2.89	6
		600–1000	0.06	H_2O [H_2O?]			
		1000–1325	1.74	SiF_4, O_2, F, HF [CO_2]			
E2335	11.419	ambient	0.06	n.a.	0.34	1.35	8
		650–900	0.08	H_2O, H_2			
		1120–1340	0.22	—			
M28173	32.019	ambient	0.17	n.a.	1.21	3.66	8
		510–1055	0.23	H_2O, H_2, CO_2			
		1055–1350	0.80	O_2, SiF_4, CO_2, [HF]			
Cardiff	25.527	ambient	0.04	n.a.	2.68	3.57	10
		500–785	0.06	H_2, H_2O [CO_2, F, HF]			
		785–1320	2.08	SiF_4, O_2, F, HF, H_2, CO_2, H_2O?			

Note: The ? = Questionable, at the limits of detection; [. . .] = very minor species.

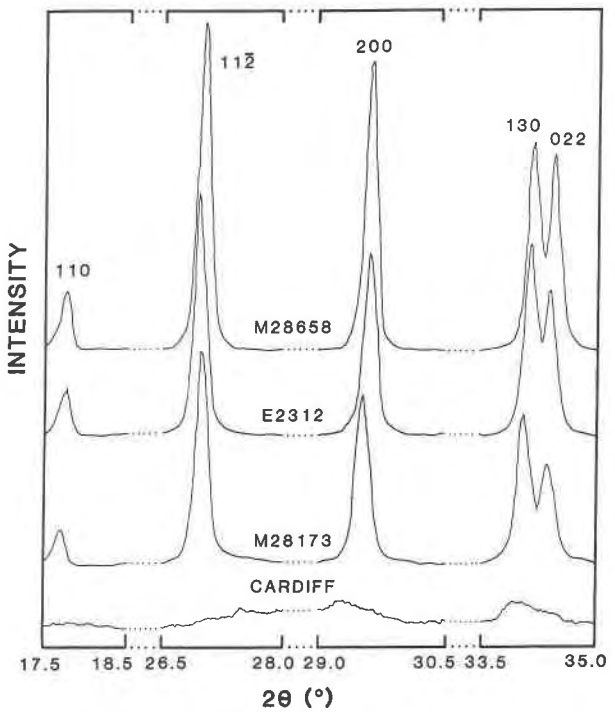

Fig. 5. X-ray diffraction patterns of titanite samples M28658, E2312, M28173, and Cardiff, showing the gradual loss of detail with increasing metamictization. Only parts of the patterns are shown, with regions of background, weak peaks, or both, omitted.

tion pattern degradation (Fig. 5). These samples were used for further work.

In many studies of metamict minerals, the samples are heated to restore crystallinity. Figure 6 shows the powder diffraction patterns for both unheated and annealed Car-

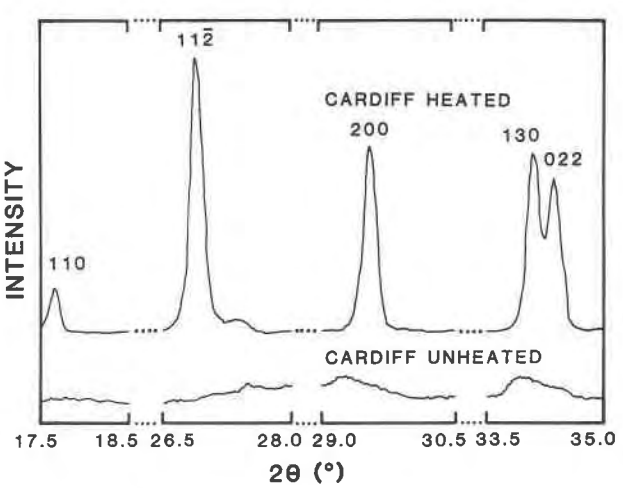

Fig. 6. X-ray diffraction patterns of heated and unheated Cardiff titanite; as in Figure 5, the complete patterns are not shown.

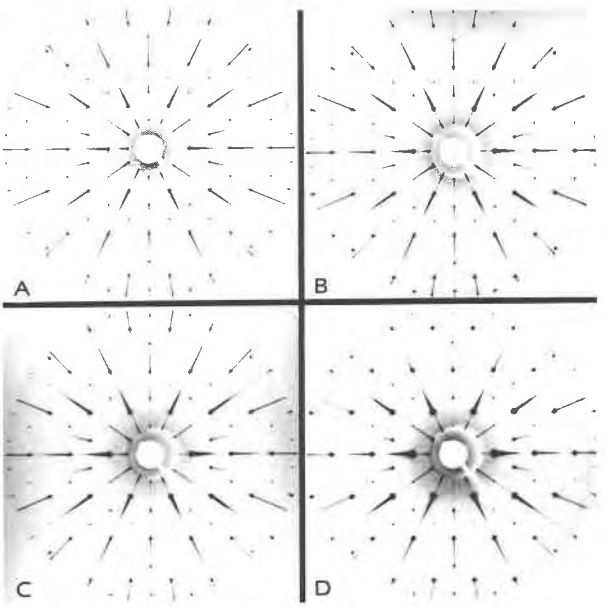

Fig. 7. X-ray zero-level **a*b*** photographs (identical exposure times) for the four titanite samples (**A**) M28658, (**B**) E2312, (**C**) M28173, and (**D**) Cardiff; **a*** is horizontal. There is progressively increasing spot size with increasing metamictization.

diff titanite; as is apparent, the titanite structure seems to be completely restored (except for a small extraneous peak in the pattern at ~25° 2θ).

Zero-level single-crystal precession photographs for these four samples are shown in Figure 7. The diffraction maxima are sharp for sample M28658 and become broader and more diffuse through the sequence E2312 → M28173 → Cardiff, following the sequence recorded in the powder diffraction data. Note also that there are no visible diffraction maxima violating the *C*-centering criterion in any of the photographs. Densitometer traces across diffraction spots in each of the zero-level photographs (Fig. 8) quantitatively confirm the visual evidence of the photographs: there is a gradual increase in spot diameter with increasing α-decay damage. Thus, both powder and single-crystal data indicate that there is a gradual decrease in degree of crystallinity in the sequence of samples given in Table 1.

There is another interesting observation to be made from a comparison of the powder and single-crystal diffraction data. The powder X-ray diffraction pattern for the Cardiff sample suggests that the material is noncrystalline, whereas the single-crystal photographs indicate a fairly high degree of crystallinity. Conversely, both the powder diffraction patterns and the single-crystal photographs for the other samples indicate crystalline material. The key difference here is that the powder diffraction samples were ground to a powder, whereas a single crystal was used for the precession photography. As the samples were uniformly prepared for powder diffraction, this sug-

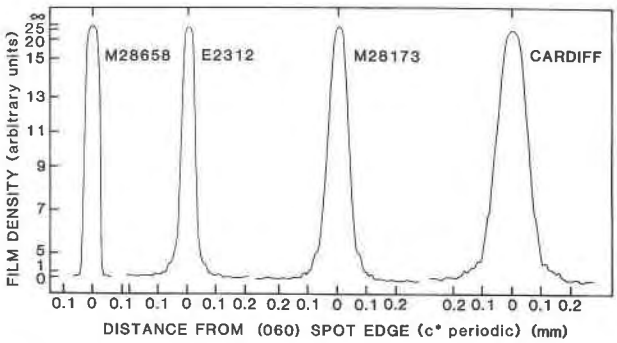

Fig. 8. Densitometer traces across a typical reflection in the zero-level precession photographs of the four titanite samples; legend is the same as that in Figure 7.

gests that the Cardiff sample may be more susceptible to grinding damage than the other samples.

Infrared spectroscopy

In the 1200–400 cm^{-1} region, the infrared spectra show a variation in sharpness and resolution similar to that shown by the X-ray powder diffraction results. The samples were ordered in terms of increasing lack of resolution, and the sequence essentially follows that derived from the powder X-ray diffraction results; there is some minor variation in sequence between the two sets of results (Table 1). The spectra in this region for samples M28658, E2312, M28173, and Cardiff are shown in Figure 9. The powder spectrum of M28658, the least metamict of the titanite samples examined, shows considerable fine detail. A prominent absorption envelope with some finer detail occurs in the region 1000–800 cm^{-1}; this may be assigned to Si-O stretching modes of the silicate tetrahedron (McMillan and Hofmeister, 1988). At lower wavenumbers, there is a broad and prominent band centered on 670 cm^{-1} and a weaker but sharper band at ~560 cm^{-1}; below this band is a series of fairly sharp bands down to 400 cm^{-1}. The assignment of these bands is not straightforward, and it is usually not possible to assign bands confidently to specific internal modes because of strong coupling effects.

With increasing degree of metamictization, the bands in the spectra lose definition, become undetectable, or both. The envelope caused by the Si-O stretching vibrations loses detail with only small amounts of damage, and its intensity is also decreased (Fig. 9). The most prominent and rapid spectral change with increase in metamict character is the loss of the broad band centered at 670 cm^{-1} (cf. M28658 and E2312, Fig. 9). The sharp band at 560 cm^{-1} is much more persistent; it does broaden somewhat and lose relative intensity, but it is still discernable in the Cardiff spectrum (Fig. 9). The same behavior is shown by the lower frequency bands.

Heating the Cardiff sample seemed to restore the titanite structure with respect to X-ray powder diffraction. As shown in Figure 10, heating the Cardiff titanite does

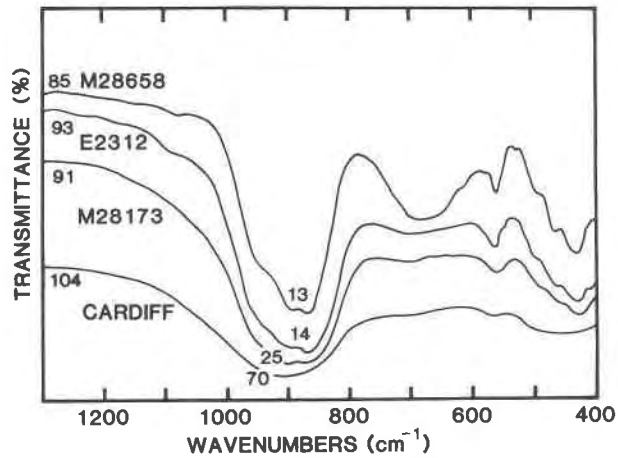

Fig. 9. Powder infrared spectra for titanite samples in the 1200–800 cm^{-1} region. Scales are the same for all spectra, which have been offset for clarity. The numbers on each spectrum indicate the background and minimum intensities.

not have as much effect on the infrared spectrum. The Si-O stretching bands are virtually unchanged, and the 670 cm^{-1} band is not restored. However, the 560-cm^{-1} band is restored (although it is less sharp than in the nonmetamict samples) together with some detail to lower frequencies. In addition, a notable band appears at ~620 cm^{-1}; this band is not present (or present only very weakly) in the spectra of undamaged samples. Thus, although the spectrum does show increased detail, it is not restored to the form shown by such samples as M28658 (Fig. 9). As X-ray diffraction and infrared absorption spectroscopy have distinctly different coherence lengths, this observation is of considerable significance with regard to the annealing process.

Most of the powder spectra show absorption in the region 3200–3700 cm^{-1}, indicative of OH, H_2O, or both, in the structure. Single-crystal spectra in the principal OH-

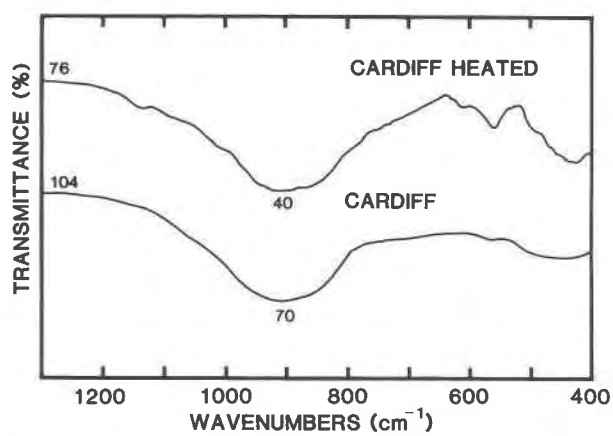

Fig. 10. Powder infrared spectra of heated and unheated Cardiff titanite in the 1200–400 cm^{-1} region; legend is the same as that in Figure 9.

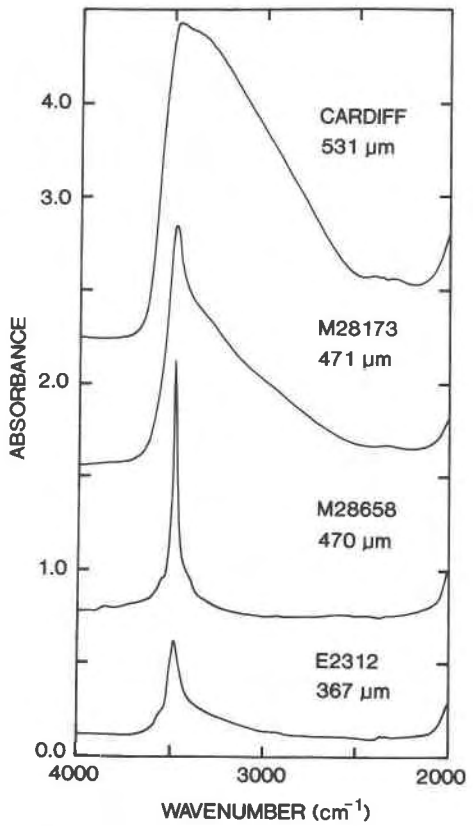

Fig. 11. Single-crystal infrared spectra of titanite in the OH region, showing the development of a low-energy wing with increasing metamictization.

stretching region (3800–2500 cm^{-1}) are shown in Figure 11. None of the spectra show a detectable band corresponding to the ν_2 bending vibrational mode of H_2O at ~1650 cm^{-1}, and there are no H_2O combination bands in the 5250 cm^{-1} region. This indicates that the H is not present as H_2O, either in the crystalline or in the metamict titanite. The most crystalline sample (M28658) shows sharp absorption at 3486 cm^{-1}; the narrow half-width and polarization dependence are indicative of OH, the results agreeing with those of Beran (1970). With increasing damage to the samples (as measured from the powder diffractograms), the sharpness of the absorption band gradually decreases and a wide wing appears to the low-energy side of the absorption, similar to the absorption in radiation-damaged zircon (Aines and Rossman, 1986). In addition, there is a weak shoulder at 3560 cm^{-1} in the spectra of M28658 and E2312; this may be assigned to OH with Al-Fe^{3+} as one of the next-nearest neighbors. The decrease in M-OH bond-valence contribution caused by this configuration is compensated by an increase in the O-H bond-valence which causes a shift in the principal OH-stretching frequency to higher values. In the more damaged samples (Cardiff and M28173), the high-frequency side of the major band is shifted to slightly higher frequencies, possibly obscuring any contribution from the weak high-frequency Al-Fe^{3+} component.

Crystal structure refinement

Scattering curves for neutral atoms and coefficients of anomalous dispersion were taken from the *International Tables for X-ray Crystallography* (1974). The *R* indices are of the form shown in Table 4 and are expressed as percentage

Using the parameters of Mongiorgi and Riva de Sanseverino (1968) as input, structures refined rapidly to convergence for an isotropic displacement model. Conversion to an anisotropic displacement model and full-matrix refinement of all variables resulted in convergence at *R* indices given in Table 4. Final parameters are listed in Table 7, structure factor tables (Table 8) are deposited, and selected interatomic distances and angles are given in Table 9.

Mössbauer spectroscopy

The spectral fitting was done with the least-squares program MOSFT (Dollase, 1975). Initial fitting was done using fully Lorentzian peak shapes. Starting parameters for the background, peak positions, half-widths, and relative intensities were estimated from inspection of the raw spectra. For the spectra of the annealed titanite, a one-doublet fit was adequate, and peak areas and half-widths of the doublet components were each constrained to be equal. In the spectra of the unannealed titanite, the spectral envelopes indicated the presence of two doublets with approximate parameters characteristic of Fe^{3+} and Fe^{2+}, respectively. For these two-doublet spectra, intensities of doublet components were constrained to be equal, and all half-widths were also constrained to be equal. The Mössbauer parameters were calibrated using Fe foil. Final parameters are given in Table 10, and the spectra are shown in Figure 12.

Magic-angle spinning NMR

Spectra for titanite sample M28658 and a synthetic end-member titanite sample (BLS406) are shown in Figure 13; each has a central ^{29}Si MAS-NMR peak with spinning sidebands. The peak widths of the titanite samples vary tremendously (Table 11), from 80 Hz for the synthetic titanite sample through 403 Hz for M28658 to approximately 1400 Hz for E2312 and M28173. In particular, the latter spectra also have intense spinning sidebands. The metamict sample (Cardiff) gave no spectrum whatsoever.

The Fe contents of the various samples, together with the MAS-NMR parameters, are listed in Table 11. It is immediately apparent that the peak-width at half-height correlates strongly with the Fe content expressed as Fe per formula unit. However, the situation must be more complex than this, as samples M28173 and Cardiff both have approximately the same amount of Fe expressed as Fe_2O_3; and yet sample M28173 had a ^{29}Si MAS-NMR signal (albeit broad), whereas Cardiff titanite gave no sig-

TABLE 7. Atomic parameters* for natural and heated titanite

	x	y	z	*U_{equiv}	**U_{11}	U_{22}	U_{33}	U_{23}	U_{13}	U_{12}
					M28658					
Ca	0	0.1677(1)	¾	155(3)	72(4)	71(4)	254(5)	0	−5(4)	0
	0	0.1681(1)	¾	142(3)	70(4)	55(4)	233(5)	0	−10(3)	0
Ti	0	½	0	111(3)	47(4)	81(4)	178(5)	45(3)	17(3)	−2(2)
	0	½	0	91(3)	48(4)	59(4)	145(4)	47(2)	18(3)	1(2)
Si	0	0.1828(1)	¼	58(4)	42(5)	59(5)	70(5)	0	19(4)	0
	0	0.1830(1)	¼	46(3)	46(5)	34(4)	55(5)	0	17(4)	0
O(1)	0	0.5714(3)	¼	90(9)	118(14)	83(13)	82(12)	0	55(11)	0
	0	0.5706(3)	¼	86(7)	145(11)	71(10)	58(9)	0	56(8)	0
O(2)	0.1855(3)	0.0663(2)	0.4102(3)	90(7)	57(9)	90(9)	110(9)	17(7)	20(7)	7(8)
	0.1854(3)	0.0666(2)	0.4107(2)	84(5)	65(7)	71(8)	99(7)	10(6)	15(6)	5(5)
O(3)	0.1025(3)	0.2893(2)	0.1185(3)	84(7)	68(10)	88(9)	98(9)	8(8)	37(8)	1(8)
	0.1024(2)	0.2896(2)	0.1177(2)	66(5)	64(7)	64(7)	74(7)	33(5)	31(6)	22(5)
					E2312					
Ca	0	0.1675(1)	¾	187(2)	90(3)	72(3)	309(4)	0	−13(4)	0
	0	0.1673(1)	¾	159(2)	76(3)	61(3)	269(4)	0	−5(2)	0
Ti	0	½	0	119(2)	72(2)	87(3)	174(3)	41(2)	25(2)	0(2)
	0	½	0	94(2)	47(3)	64(3)	152(3)	44(1)	21(2)	−1(1)
Si	0	0.1830(2)	¼	70(3)	65(3)	64(4)	78(3)	0	25(3)	0
	0	0.1832(1)	¼	57(2)	52(3)	50(3)	69(3)	0	24(3)	0
O(1)	0	0.5719(2)	¼	97(7)	127(9)	81(9)	87(9)	0	47(8)	0
	0	0.5717(2)	¼	72(5)	102(8)	56(7)	72(7)	0	49(6)	0
O(2)	0.1855(2)	0.0665(2)	0.4104(2)	113(5)	82(7)	107(7)	126(7)	18(5)	15(5)	6(6)
	0.1857(2)	0.0665(2)	0.4108(2)	89(4)	70(5)	71(6)	112(5)	12(4)	24(4)	5(4)
O(3)	0.1027(2)	0.2897(2)	0.1186(2)	105(5)	98(7)	93(6)	128(7)	18(6)	52(6)	9(6)
	0.1030(2)	0.2896(1)	0.1188(2)	77(4)	76(6)	65(5)	94(5)	15(4)	39(4)	8(4)
					M28173					
Ca	0	0.1686(1)	¾	212(4)	105(4)	86(5)	336(6)	0	−22(4)	0
	0	0.1678(1)	¾	145(3)	61(4)	58(4)	240(5)	0	−18(3)	0
Ti	0	½	0	151(3)	105(4)	123(4)	200(4)	36(3)	36(3)	4(3)
	0	½	0	95(3)	55(4)	76(4)	134(4)	36(2)	18(3)	−1(2)
Si	0	0.1827(1)	¼	94(4)	94(5)	84(6)	102(6)	0	36(4)	0
	0	0.1828(1)	¼	64(3)	60(5)	58(4)	71(5)	0	22(4)	0
O(1)	0	0.5717(4)	¼	143(11)	163(15)	124(16)	138(15)	0	57(13)	0
	0	0.5727(3)	¼	89(7)	111(10)	89(10)	65(9)	0	35(8)	0
O(2)	0.1851(4)	0.0660(3)	0.4103(4)	156(8)	117(10)	149(11)	170(11)	19(9)	24(9)	−4(9)
	0.1850(3)	0.0658(2)	0.4113(2)	99(5)	84(7)	105(8)	96(7)	21(5)	25(6)	11(5)
O(3)	0.1033(4)	0.2895(3)	0.1188(3)	144(7)	130(11)	130(1)	169(11)	22(9)	60(9)	16(9)
	0.1035(3)	0.2892(2)	0.1187(3)	95(5)	104(8)	84(8)	110(8)	27(5)	59(6)	10(6)
					Cardiff					
Ca	0	0.1687(2)	¾	367(7)	173(8)	165(8)	566(13)	0	−41(8)	0
	0	0.1669(2)	¾	95(6)	16(8)	1(7)	194(10)	0	−33(7)	0
Ti	0	½	0	306(6)	202(7)	245(8)	405(10)	49(7)	56(6)	15(6)
	0	½	0	85(5)	39(7)	53(8)	144(8)	−1(6)	18(6)	49(6)
Si	0	0.1835(3)	¼	212(7)	171(10)	190(10)	241(11)	0	49(8)	0
	0	0.1835(3)	¼	17(7)	23(10)	10(10)	24(10)	0	16(8)	0
O(1)	0	0.5709(7)	¼	257(20)	227(27)	218(29)	283(30)	0	61(23)	0
	0	0.5725(7)	¼	34(16)	70(25)	18(26)	1(23)	0	0	0
O(2)	0.1859(7)	0.0664(5)	0.4094(7)	292(15)	217(22)	274(22)	316(23)	26(19)	39(17)	−7(17)
	0.1877(7)	0.0668(5)	0.4115(7)	47(14)	7(18)	54(20)	65(20)	−9(16)	0(16)	10(16)
O(3)	0.1019(6)	0.2902(5)	0.1194(7)	268(15)	198(18)	257(21)	322(23)	31(18)	79(17)	33(16)
	0.1034(7)	0.2904(5)	0.1186(7)	35(13)	32(18)	19(18)	59(19)	12(15)	23(16)	15(16)

* The lower set of data is for the heated crystals.
** $U_{ij} = U_{ij} \times 10^4$.

nal at all. The reason for this could lie in the different valence states of Fe in the different samples. Natural titanite usually has Fe present in the trivalent state. However, the Mössbauer spectrum for Cardiff titanite shows that Fe is present in both divalent and trivalent states, with significant Fe^{2+} in the metamict material. Sherriff (1984) has shown that Fe^{2+} causes more severe paramagnetic quenching than Fe^{3+} in pyroxene. If this is the general case, then the lack of signal in the Cardiff sample can be rationalized by the presence of significant amounts of Fe^{2+} in the structure. Alternatively, it is possible that the quenching is enhanced by paramagnetic defects associated with increasing radiation damage.

High-resolution transmission electron microscopy

Single-crystal electron diffraction patterns of the nonmetamict titanite samples are intense (Fig. 14a) and lack the diffuse halos that are usually associated with radiation damage. However, weak streaks were observed between $h + k = 2n$ diffraction spots, which is consistent with an average structure transitional between space groups $P2_1/c$ and $C2/c$ (Higgins and Ribbe, 1976). The bright-field image (Fig. 14b) is typical of undamaged material, and continuous lattice fringes are observed over large areas in HRTEM images taken near thin edges (Fig. 14c).

Electron diffraction patterns of sample M28173 gen-

TABLE 9. Selected interatomic distances (Å) and angles (°) in natural and heated titanite

		M28659		E2312		M28173		Cardiff	
		Natural	Heated	Natural	Heated	Natural	Heated	Natural	Heated
Si-O(2)	×2	1.633(2)	1.633(2)	1.637(1)	1.636(2)	1.638(2)	1.638(2)	1.647(4)	1.640(4)
Si-O(3)	×2	1.635(2)	1.636(2)	1.640(2)	1.636(2)	1.640(3)	1.635(2)	1.644(5)	1.637(6)
⟨Si-O⟩		1.634	1.635	1.639	1.636	1.639	1.637	1.646	1.639
O(2)-O(2)a		2.564(3)	2.564(3)	2.569(2)	2.566(3)	2.566(4)	2.566(3)	2.574(7)	2.582(8)
O(2)-O(3)	×2	2.718(3)	2.720(2)	2.726(2)	2.720(3)	2.725(3)	2.725(2)	2.735(7)	2.721(7)
O(2)-O(3)a	×2	2.654(3)	2.652(2)	2.662(2)	2.657(3)	2.666(3)	2.657(2)	2.682(6)	2.663(7)
O(3)-O(3)a		2.695(5)	2.696(4)	2.703(4)	2.698(4)	2.701(5)	2.696(4)	2.702(7)	2.698(9)
⟨O-O⟩Si		2.667	2.667	2.675	2.670	2.675	2.671	2.685	2.675
O(2)-Si-O(2)a		103.4(1)	103.5(1)	103.3(1)	103.3(1)	103.2(2)	103.1(1)	102.8(3)	103.8(3)
O(2)-Si-O(3)	×2	112.5(1)	112.5(1)	112.6(1)	112.5(1)	112.5(1)	112.7(1)	112.4(2)	112.3(2)
O(2)-Si-O(3)a	×2	108.6(1)	108.5(1)	108.6(1)	108.6(1)	108.8(1)	108.5(1)	109.2(2)	108.7(3)
O(3)-Si-O(3)a		111.0(2)	111.0(1)	111.0(1)	111.1(1)	110.9(2)	111.1(1)	110.5(4)	111.0(4)
⟨O-Si-O⟩		109.4	109.4	109.4	109.4	109.4	109.4	109.4	109.5
Ti-O(1)	×2	1.871(1)	1.863(1)	1.877(1)	1.872(1)	1.871(1)	1.871(1)	1.883(2)	1.871(2)
Ti-O(2)b	×2	1.980(2)	1.979(2)	1.983(2)	1.978(2)	1.987(2)	1.981(2)	1.992(4)	1.963(5)
Ti-O(3)	×2	2.013(2)	2.008(1)	2.015(1)	2.012(2)	2.018(2)	2.016(1)	2.024(4)	2.001(4)
⟨Ti-O⟩		1.955	1.950	1.958	1.954	1.959	1.956	1.966	1.945
O(1)-O(2)b	×2	2.722(3)	2.718(2)	2.729(2)	2.724(2)	2.728(3)	2.724(2)	2.743(5)	2.709(6)
O(1)-O(2)d	×2	2.726(2)	2.719(2)	2.732(2)	2.723(2)	2.732(3)	2.725(2)	2.741(6)	2.715(5)
O(1)-O(3)	×2	2.798(3)	2.790(3)	2.806(2)	2.800(2)	2.807(4)	2.810(3)	2.809(7)	2.795(7)
O(1)-O(3)c	×2	2.697(2)	2.688(2)	2.700(2)	2.694(2)	2.697(3)	2.689(2)	2.720(6)	2.683(6)
O(2)d-O(3)	×2	2.819(3)	2.813(2)	2.821(2)	2.817(2)	2.833(3)	2.827(2)	2.826(5)	2.797(6)
O(2)d-O(3)c	×2	2.829(3)	2.826(2)	2.833(2)	2.826(2)	2.831(3)	2.825(2)	2.850(7)	2.810(7)
⟨O-O⟩Ti		2.765	2.759	2.770	2.764	2.771	2.766	2.781	2.752
O(1)-Ti-O(2)b	×2	89.9(1)	90.0(1)	89.9(1)	90.0(1)	89.9(1)	90.0(1)	90.0(1)	89.9(2)
O(1)-Ti-O(2)d	×2	90.1(1)	90.0(1)	90.1(1)	90.0(1)	90.1(1)	90.0(1)	90.0(1)	90.1(2)
O(1)-Ti-O(3)	×2	92.1(1)	92.2(1)	92.2(1)	92.2(1)	92.3(1)	92.5(1)	91.9(2)	92.3(2)
O(1)-Ti-O(3)c	×2	87.9(1)	87.8(1)	87.8(1)	87.8(1)	87.7(1)	87.5(1)	88.1(2)	87.7(2)
O(2)d-Ti-O(3)	×2	89.8(1)	89.7(1)	89.8(1)	89.8(1)	90.0(1)	90.0(1)	89.7(2)	89.7(2)
O(2)d-Ti-O(3)c	×2	90.2(1)	90.3(1)	90.2(1)	90.2(1)	90.0(1)	90.0(1)	90.3(2)	90.3(2)
⟨O-Ti-O⟩		90.0	90.0	90.0	90.0	90.0	90.0	90.0	90.0
Ca-O(1)e		2.269(3)	2.271(2)	2.271(2)	2.269(2)	2.265(3)	2.257(2)	2.286(6)	2.261(7)
Ca-O(2)f	×2	2.405(2)	2.409(2)	2.410(1)	2.404(2)	2.415(2)	2.403(2)	2.431(5)	2.404(5)
Ca-O(3)a	×2	2.631(2)	2.620(2)	2.639(2)	2.634(2)	2.630(2)	2.627(2)	2.655(5)	2.632(5)
Ca-O(3)g	×2	2.413(2)	2.410(1)	2.415(1)	2.408(2)	2.414(2)	2.405(2)	2.433(4)	2.400(4)
⟨Ca-O⟩		2.452	2.450	2.457	2.451	2.455	2.447	2.473	2.448

Note: Equivalent positions: (a) = $-x, y, \frac{1}{2} - z$; (b) = $\frac{1}{2} - x, \frac{1}{2} + y, \frac{1}{2} - z$; (c) = $-x, 1 - y, -z$; (d) = $-\frac{1}{2} + x, \frac{1}{2} - y, -\frac{1}{2} + z$; (e) = $x, 1 - y, 1 - z$; (f) = $-x, -y, 1 - z$; (g) = $\frac{1}{2} - x, \frac{1}{2} - y, 1 - z$.

erally lack both streaking between reflections for which $h + k = 2n$ and diffuse halos (Figs. 15a, 15c), suggesting that the average structure is based on space group $C2/c$ and is largely undamaged. However, bright-field images show mottled diffraction contrast (Fig. 15b), which is typical of the early stages of α-recoil damage (Lumpkin and Ewing, 1988). Despite the mottled contrast, HRTEM images show the lattice fringes to be largely continuous (Figs. 15d, 15e). This is the earliest stage of α-recoil damage recognizable by TEM. Mottled contrast at this stage probably results from strain fields and Frenkel defects around isolated α-recoil and α-particle tracks.

The Cardiff sample shows a diffuse halo at 3.00 Å in electron diffraction patterns (Figs. 16a, 16b). The strong mottled diffraction contrast in bright-field images (Fig. 16c) is further evidence of moderate α-recoil damage. HRTEM images show that the mottled contrast results from coexisting crystalline and aperiodic domains produced by overlapping α-recoil tracks. Most aperiodic domains are within the size range 20–100 Å. The microstructural features of Cardiff titanite are consistent with radiation damage on the order of 30–50% of that required to render the structure fully aperiodic (Lumpkin and Ewing, 1988). However, some areas of the sample

TABLE 10. Mössbauer parameters for natural and heated titanite

	Fe^{3+}				Fe^{2+}					
	QS	IS	HW	AR	QS	IS	HW	AR	CHI	MSFT
M28173	1.27(2)	0.33(2)	0.45(1)	0.95(1)	2.16(8)	1.12(8)	0.33(2)	0.05(1)	0.46	1.34
M28183H	1.17(2)	0.35(2)	0.44(1)	1.00	—	—	—	—	0.48	2.24
M28696	1.13(2)	0.38(2)	0.58(2)	0.55(5)	2.09(7)	1.04(8)	0.34(3)	0.45(5)	0.66	3.94
M28696H	1.02(2)	0.35(1)	0.46(1)	1.00	—	—	—	—	0.61	2.12

Note: QS = quadrupole splitting (mm/s); IS = isomer shift (mm/s, relative to Fe foil); HW = halfwidth (mm/s); AR = area ratio (as a percentage); CHI = chi-squared/channel; MSFT = MISFIT parameter.

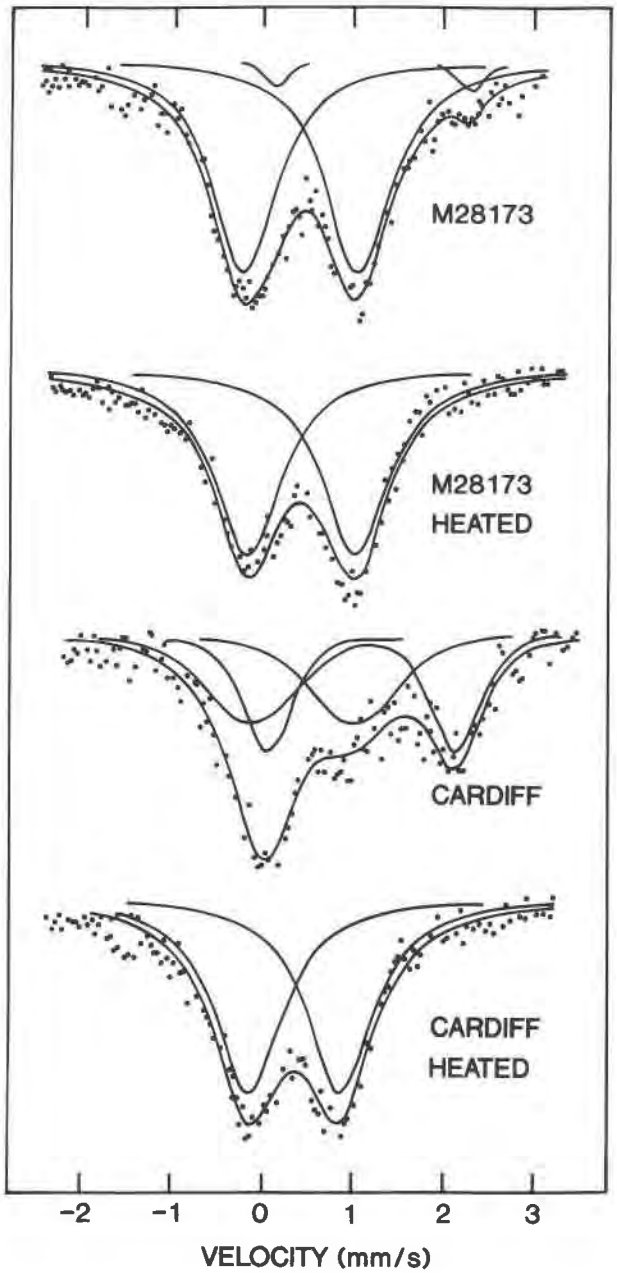

Fig. 12. Mössbauer spectra of partially metamict titanite.

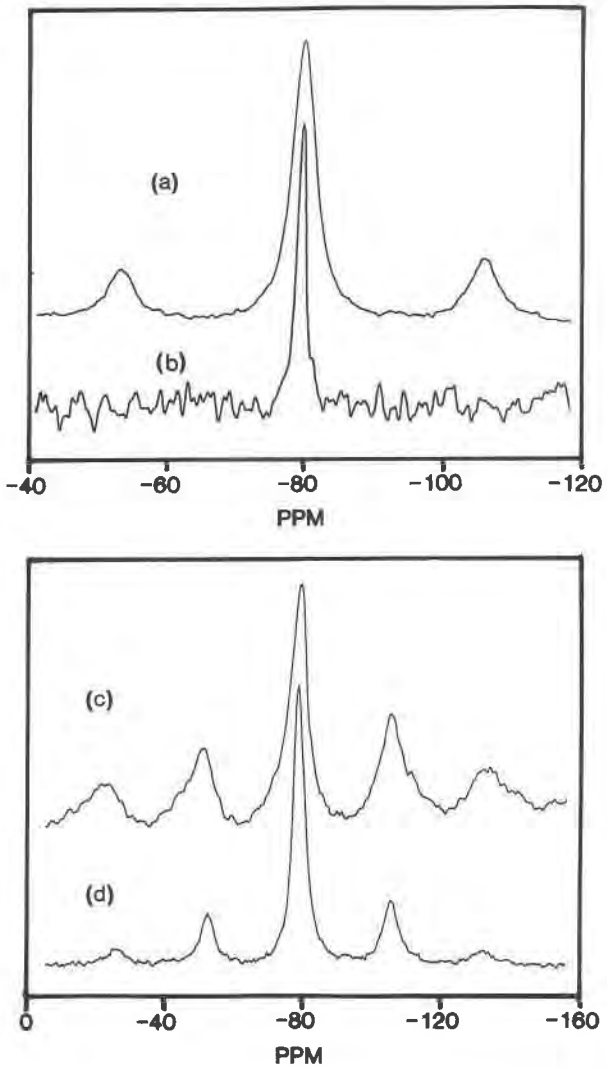

Fig. 13. MAS-NMR spectra of a synthetic titanite and three natural titanite samples: (a) M28658, (b) synthetic titanite, (c) M28173, and (d) E2312. The Cardiff sample gave no signal.

seem more highly damaged, with small randomly oriented crystallites (Fig. 17); the SAED pattern (see inset, Fig. 17) shows diffuse rings and rather spotty rings. The microstructure observed here is interpreted as recrystallization through low-temperature natural annealing.

EXAFS and XANES spectroscopy

The results of the Ti*K* edge XANES measurements for the most highly crystalline titanite sample (M28658), the most radiation-damaged titanite sample (Cardiff), and titanite glass (Eganville, Ontario titanite) are given in Figure 18. The most notable aspect of the EXAFS spectra is the increase in intensity of the pre-edge feature at approximately +5 eV above the Ti*K* edge at 4966.4 eV. In a detailed study of Ti XANES spectra in minerals, Waychunas (1987) showed that the pre-edge features often

Table 11. ^{29}Si MAS-NMR parameters for titanite

Titanite	^{29}Si chemical shift (ppm)	Peak halfwidth (Hz)	Fe* (pfu)
Synthetic	−78.9(1)	80 (10 Hz LB)	—
M28658	−78.9(1)	403 (50 Hz LB)	0.06
E2312	−75(5)	1300 (100 Hz LB)	0.29
M28173	−74(5)	1400 (100 Hz LB)	0.37
Cardiff	no signal		0.36
Calculated**	−80.9		

* For 20 anions.
** From Sherriff and Grundy (unpublished data).

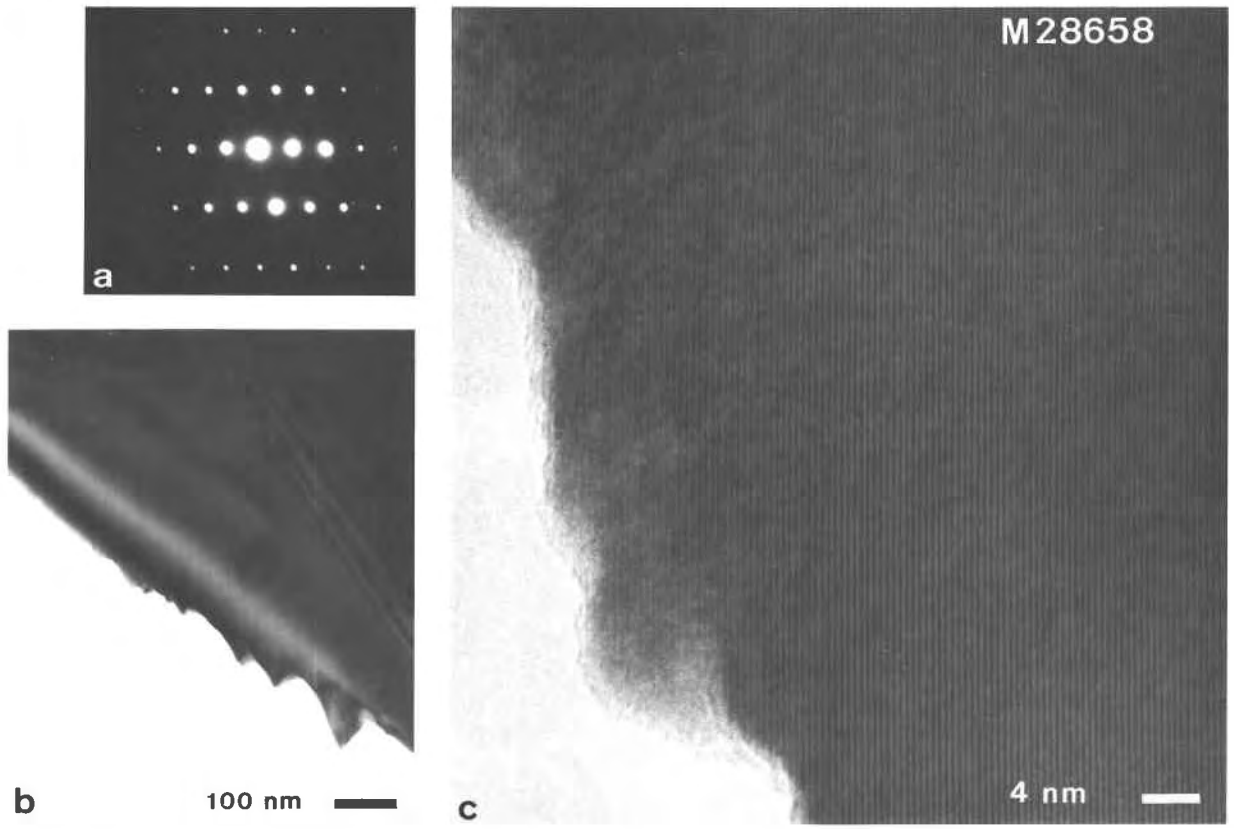

Fig. 14. Titanite sample M28658: (**a**) selected area electron diffraction pattern ([201] zone) of the grain shown in **b**, showing weak streaking between diffraction spots; (**b**) bright-field image showing extinction contours caused by thickness variation; and (**c**) HRTEM image of the edge of the grain shown in **b**.

consist of three components. Only two are visible in the spectrum of highly crystalline titanite given here (Fig. 18); this is also the case for the titanite spectrum given by Waychunas (1987). However, in the spectrum of Cardiff titanite, the α-decay damaged titanite, the first weak pre-edge feature is undetectable. The principal peak in the pre-edge feature can be assigned to the $1s \rightarrow 3d$ transition. This transition is dipole forbidden, but is allowed when the center of inversion is lost, the intensity being a function of the degree of d-p mixing that accompanies local distortion around the Ti site. Thus, the increasing intensity of the pre-edge feature with increasing α-decay damage indicates a significant departure of the Ti environment from centrosymmetry. The origin of the first weak pre-edge feature is less clear. It has been assigned to a core-hole exiton state (Grunes, 1982) and to a transition from shake-up to shake-off involving the normally filled $1t_{1g}$ state during formation of a core hole (Greegor et al., 1983). It is clear that this feature becomes undetectable with increasing α-decay damage, whereas the principal pre-edge peak increases in intensity (Fig. 18).

The first peak at the top of the absorption rise has been identified as a 1s-4p plus shake-down transition (Bair and Goddard, 1980). However, more recently, this peak has been shown to be caused by multiple scattering of the ejected photoelectric wave from coordinating shells around the Ti. In the same way, the second peak has been shown to be caused by scattering from first neighbor MO_6 sites (Greegor et al., 1984; Sandstrom et al., 1980). Peak positions measured with respect to the 1s-3d feature can be associated with bond lengths, the higher energy peaks corresponding to shorter bond lengths. The loss of sharpness of the doublet at the top of the absorption rise in the spectrum of the Eganville glass sample is indicative of a larger spread in bond lengths and bond angles at the $^{[6]}$Ti sites. In addition, the small but distinctive feature in the glass spectrum at +45 eV corresponds to TiO_4 bond lengths; as this environment is very noncentrosymmetric, the 1s-3d transition will be greatly enhanced at such local configurations. Thus, the pre-edge feature at +5 eV in the glass spectrum is considerably stronger than that in the spectra of the crystalline samples. However, the enhanced intensity of the +5 eV pre-edge feature in the Cardiff titanite sample is more significantly affected by local disorder around $^{[6]}$Ti sites.

The k^3 Ti-O phase-corrected Fourier transforms of the Ti*K* edge EXAFS for $k = 3$–10 Å^{-1} are shown in Figure 19; the nearest neighbors expected from the X-ray dif-

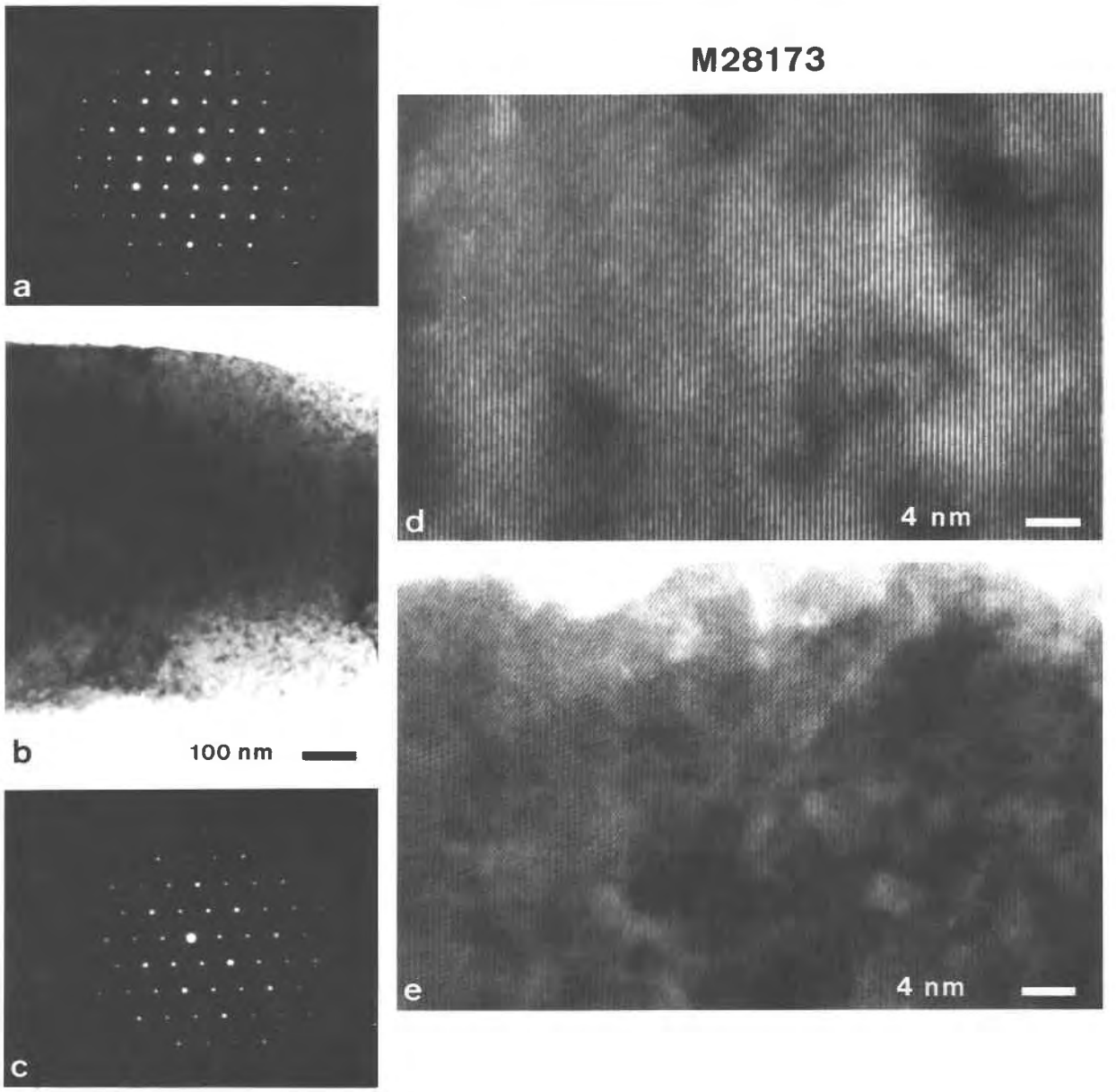

Fig. 15. Titanite sample M28173: (**a**) and (**c**) selected area diffraction patterns ([112] and [001] zones, respectively) of the grain shown in **b**; (**b**) bright-field image showing mottled diffraction contrast; (**d**) HRTEM image corresponding to the diffraction pattern in **a**; and (**e**) HRTEM image corresponding to the diffraction pattern in **c**. Both images show only limited disruption of lattice fringes.

fraction data are indicated in the figure. The radiation-damaged natural titanite sample shows a reduced magnitude for the first-neighbor Ti-O peak, indicative of a lowering of coordination number, an increase in disorder around the Ti site, or both. In addition, this transform shows a reduction in peak magnitudes for the more distant shells when compared to the most crystalline titanite, consistent with an increase in disorder in the more metamict sample. The Fourier transform for the Eganville glass sample shows the same reduction in Ti-O peak magnitude, but the peak is shifted to lower r values, indicating some fraction of the Ti to be four-coordinated. The Ti peak is comparatively broad and does not allow resolution of the separate $^{[4]}$Ti and $^{[6]}$Ti bond lengths. If the transform were taken over a broader range of k (for example 3–15 Å^{-1}) with data obtained at liquid N_2 temperature with a good signal-to-noise ratio, then the separate bond lengths could possibly be resolved. The nearest-neighbor Ti-O distances (taken from the peaks of the Fourier transforms) for the crystalline titanite sample

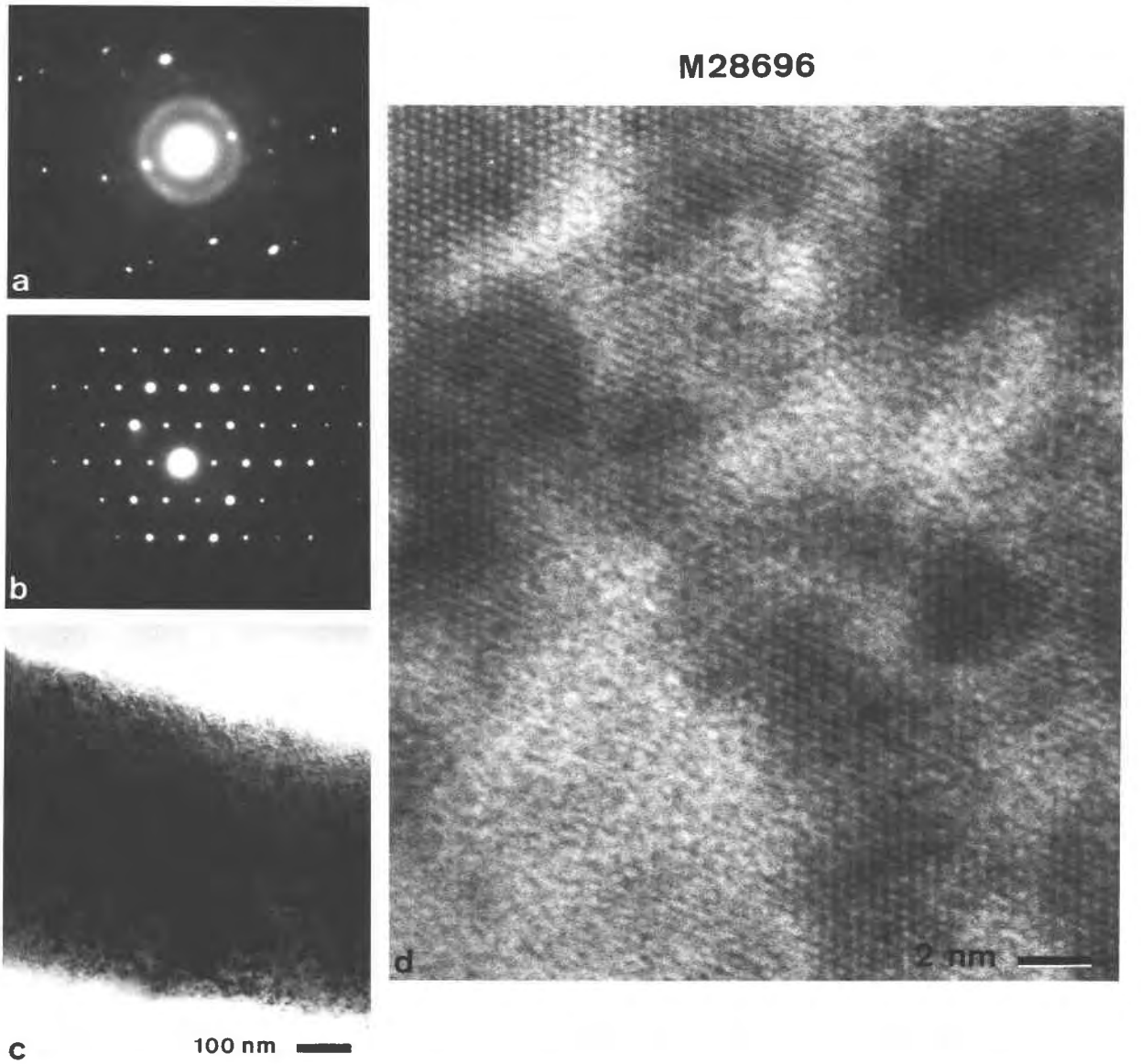

Fig. 16. Cardiff titanite sample: (**a**) diffraction pattern, tilted and exposed to show the diffuse halo at 3.00 Å; (**b**) oriented diffraction pattern ([101] zone) of the grain shown in **c**, with the diffuse halo still weakly visible; (**c**) bright-field image showing strong mottled diffraction contrast; and (**d**) HRTEM image clearly showing coexisting crystalline and aperiodic domains.

(M28658), the radiation-damaged titanite sample (Cardiff), and the Eganville titanite glass sample are 2.04(3), 2.03(3), and 1.79(3) Å, respectively. The shorter bond length for the Eganville glass sample suggests that some Ti is four-coordinated; we estimate this fraction using curve-fitting techniques as described below.

Inverse Fourier transforms of the nearest-neighbor Ti-O peaks were calculated, and these back transforms were used in nonlinear curve fitting. The back transforms and analytical fits to these spectra are shown in Figure 19. The O scattering amplitude and Ti-O phase shift were taken from anatase (TiO_2) after being tested for transferability on rutile and brookite. Single-shell fits were made to the crystalline and radiation-damaged titanite samples. A two-shell fit (both $^{[4]}$Ti and $^{[6]}$Ti) was necessary for the Eganville titanite glass sample in order to reproduce the spectrum at approximately 9 $Å^{-1}$. The bond length results for the crystalline titanite sample (M28658) and the metamict titanite sample (Cardiff) are 2.03(3) and 2.00(3) Å, respectively; these values compare well with the values obtained above from the peaks in the Fourier transforms and are also consistent with $^{[6]}$Ti. For the Eganville titanite glass sample, the bond lengths obtained are 1.75(3) Å ($^{[4]}$Ti) and 1.92(3) Å ($^{[6]}$Ti).From the two-shell fit to the glass [coordination numbers $N(4) = 0.2$, $N(6) = 5.3$], the estimated amount of $^{[4]}$Ti is 0.1(3). In all the above fits

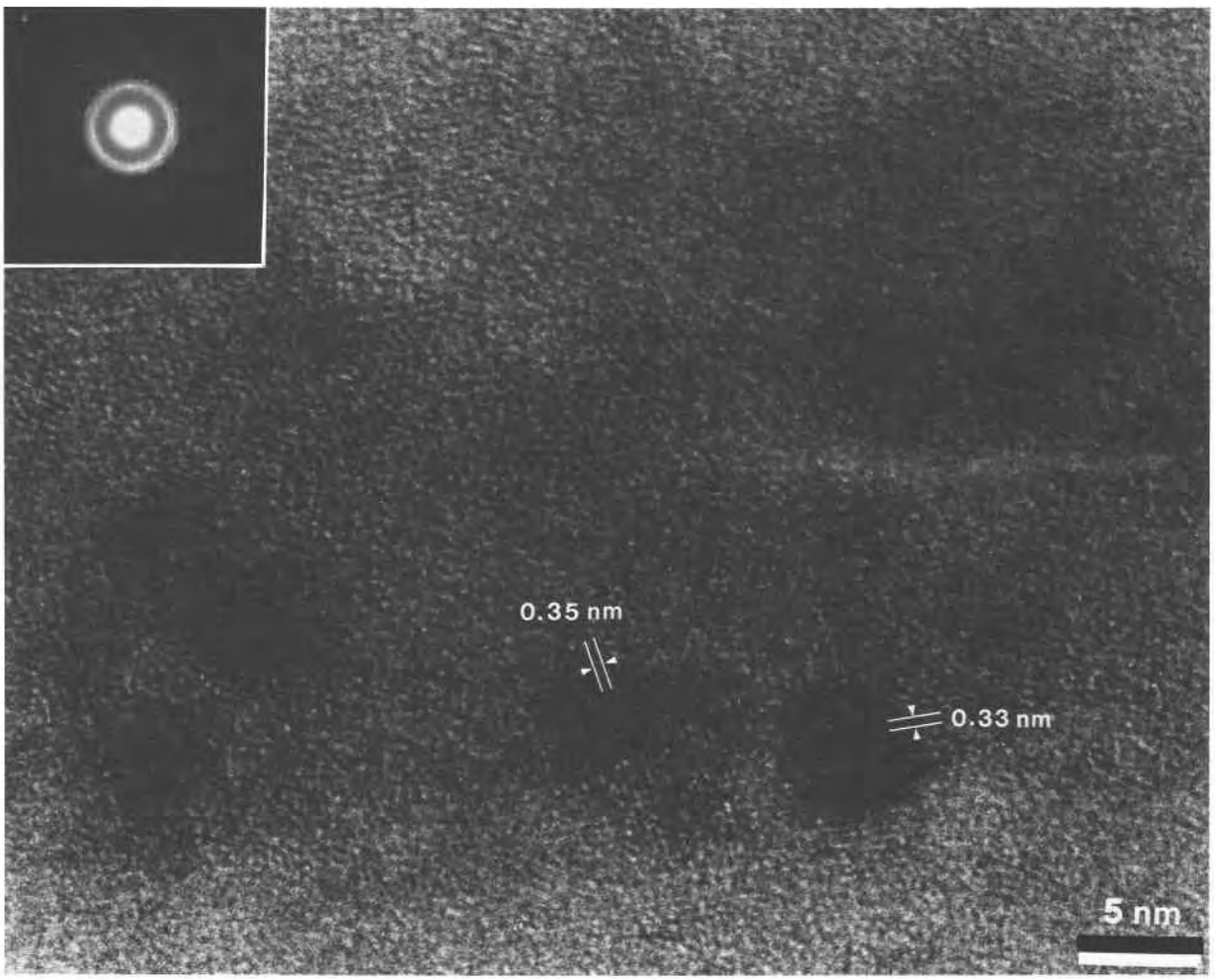

Fig. 17. Cardiff titanite sample: HRTEM image of a more highly damaged region of the sample, with randomly oriented islands of crystalline material within an aperiodic matrix. The selected area electron diffraction pattern shows diffuse and spotty rings.

to the data, the increase in the mean square relative displacement (both thermal and static) was less than 0.008 Å, as compared to the anatase standard and $\Delta E < 12.5$ eV. Although the error in the estimation of the fraction of $^{[4]}$Ti is large, it does indicate a significant difference in the structure of the glass and the radiation-damaged titanite.

Discussion

Powder diffraction

Powder diffraction patterns have long been used as a relative measure of radiation damage in periodic solids. Relative peak intensities (per unit sample weight), individual *d*-values, peak widths, profile shapes, and cell dimensions are all sensitive to radiation effects (Lumpkin and Ewing, 1988). Furthermore, these parameters have been quantitatively related to annealing temperature in heating experiments on metamict or partly metamict minerals (Vance and Metson, 1985; Murakami et al., 1986; Stout et al., 1987). Thus, the extent to which the crystalline-to-metamict transition has occurred can be estimated on the basis of the degradation of the X-ray diffraction pattern (Table 1).

A diffraction peak can be considered to have two components, a Bragg diffraction peak and a diffuse scattering component, the relative intensities of which are a function of the number of defects (Howard and Sabine, 1964). For defect-free materials, Bragg diffraction almost completely dominates the scattered X-rays. With increasing defect density, Bragg diffraction decreases in absolute intensity while the diffuse scattering component becomes more important, until for defect-rich (radiation damaged) materials, the diffuse scattering can exceed the Bragg diffraction contribution to an observed peak. The diffuse scattering contribution occurs at slightly higher values of 2θ than the associated Bragg diffraction, skewing the resultant diffraction envelope (Murakami et al., 1986). Increasing radiation damage is thus marked by (1) increas-

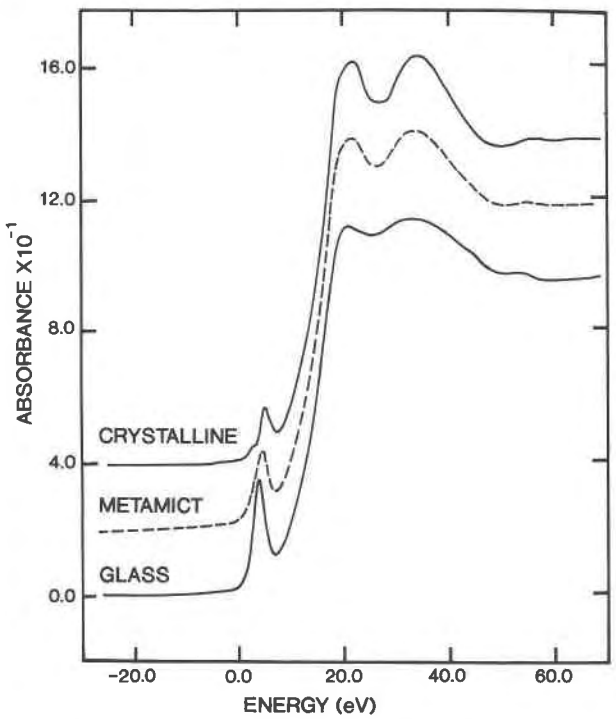

Fig. 18. Ti*K* edge XANES for crystalline (M28658), partly metamict (Cardiff), and glassy titanite samples. The zero of energy is taken at the Ti*K* edge.

ing peak asymmetry, with maximum intensity skewed to low 2θ values; (2) increasing half-widths of the composite peaks; and (3) loss of Bragg diffraction intensity. Figure 4 shows this for the titanite samples examined here. As the 330 α_1-α_2 doublet decreases in intensity (for the same weight of sample), the peak profile becomes wider and shows an increasing skew to low 2θ values, indicative of a decreasing Bragg component and an increasing diffuse scattering component. Much of this skewing is lost upon heating (Fig. 6) as the Bragg diffraction component is restored by recrystallization. A similar feature is evident in the X-ray precession photographs (Fig. 7): the diffraction maxima become more diffuse (Fig. 8) with increasing α-decay dose.

Increased degree of radiation damage is also accompanied by expansion of the unit cell and, therefore, a decrease in density. There are several possible competing processes that affect unit-cell size, not all of which are directly related to metamictization:

1. The decrease in intensity of the Bragg diffractions, together with the increase in intensity of the diffuse scattering component, results in a shift of the centroid of the diffraction maxima to higher 2θ values, resulting in smaller apparent d-values and thus smaller apparent cell dimensions.

2. There is an actual expansion of the unit cell due to the introduction of interstitial defects.

3. Aperiodic solids or defect structures are more susceptible to hydration (and other forms of alteration), which leads to further expansion of the structure.

4. Metamict minerals of complex composition tend to have more components in the structure; these components may lead to expansion or contraction of (some of) the constituent coordination polyhedra relative to those observed in structures with compositions closer to the ideal composition.

The possible effects of these factors are examined in more detail here. Points 1–3 are a result of the metamictization process, whereas point 4 is (in principle) independent of any α-decay effects. If heating of the material causes complete isochemical recrystallization, then any effect of points 1 and 2 should be removed by heating; point 4 should be unaffected. Higgins and Ribbe (1976) have shown that metamict titanite does not show the same dependence of cell edges on constituent octahedral cation radius as does nonmetamict titanite. Furthermore, heating reduces the cell dimensions of the metamict varieties such that they fall on the trends for the nonmetamict samples. This indicates that deviations from the ideal $CaTiSiO_5$ stoichiometry and radiation damage both contribute to differences in cell dimensions between ideal titanite and its metamict varieties.

Constituent cation radii for the seven- and six-coordinate sites are shown in Table 12, where they are com-

Table 12. Constituent cation radii, mean bond lengths, and cell volumes for natural, heated, and synthetic titanite

	M28658	E2312	M28173	Cardiff	Syn*	Al**
⟨*r*⟩ Ti-site	0.603	0.603	0.605	†0.604	0.605	0.599
⟨Ti-O⟩	1.955	1.958	1.959	1.964	1.959	1.951
⟨Ti-O⟩ anneal	1.950	1.954	1.956	1.945	—	—
⟨*r*⟩ Ca-site	1.060	1.060	1.056	1.058	1.060	1.060
⟨Ca-O⟩	2.452	2.457	2.455	2.473	2.458	2.448
⟨Ca-O⟩ anneal	2.450	2.451	2.447	2.448	—	—
F (pfu)	0.01	0.17	0.13	0.28	0.00	0.02
V (Å^3)	367.6	368.8	369.5	375.3	370.2	365.9
V anneal (Å^3)	366.0	367.3	366.6	364.8	—	—

Note: All bond lengths and constituent ionic radii are in Å.
* Values from Speer and Gibbs (1976).
** Values from Hollabaugh and Foit (1984).
† Value for observed Fe^{2+}/Fe^{3+}; for all Fe^{3+}, ⟨*r*⟩ = 0.600.

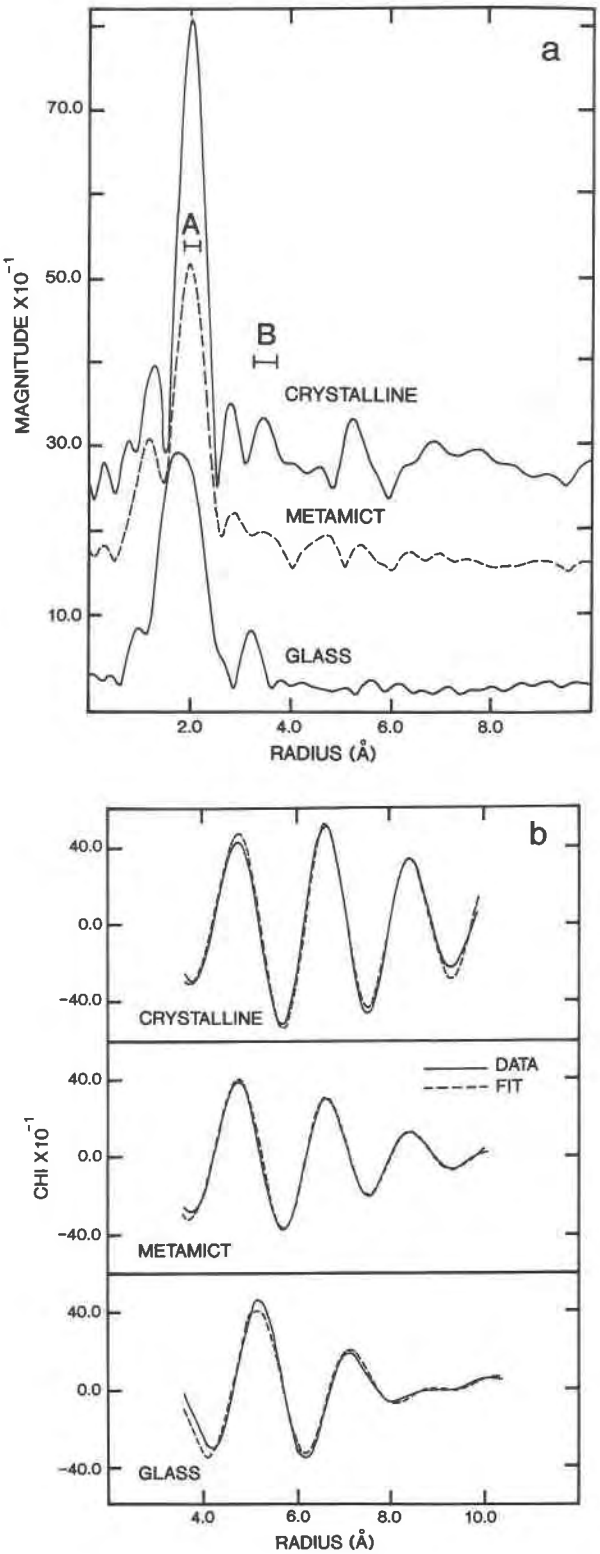

Fig. 19. (**a**) Fourier transforms of Ti*K* edge EXAFS for crystalline (M28658), partly metamict (Cardiff), anad glassy titanite samples; (**b**) nonlinear least-squares fits to first-shell Ti-O inverse Fourier transforms for the same samples. Bars mark observed mean interatomic distances in the refined crystal structures; A: Ti-O = 1.77–2.03 Å. B: Ti-NNN = 3.27–3.54 Å; NNN = 4 Si, 4 Ca, 1 O, and 2 Ti.

pared with values for pure synthetic ($P2_1/c$) titanite and natural aluminous titanite. The variation in mean constituent cation radius at the Ca and Ti sites is extremely small. If there is no relative partitioning of cations between the damaged and undamaged regions, then the span of constituent cation radius at the Ti site is 0.002 Å. This assumption may not be valid for the Cardiff sample. If the presence of Fe^{2+} in the structure is the result of radiation damage (as we argue elsewhere), then the Fe^{2+} may occur preferentially in damaged (noncrystalline) regions, and the constituent cation radius at the Ti site may be reduced. However, even if this partitioning is complete, it will reduce the constituent cation radius by only 0.005 Å (Table 12), a small amount. The corresponding variation in the constituent cation radius at the Ca site is similarly small (with a maximum departure from the ideal value of only 0.004 Å). In addition, for the Cardiff titanite, all of the substitutions act so as to reduce rather than increase the cell dimensions. Thus, these data indicate that the significant variation in cell parameters is not a structural response to compositional variation at the cation sites. There is also the possibility of anion substitution at the O(1) site bridging the Ti octahedra: both $(OH)^-$ and F^- may substitute for O^{2-}. The maximum F occupancy of this site is 0.28 in the Cardiff sample; this will reduce the constituent O(1) anion radius by 0.017 Å, reducing ⟨Ti-O⟩ and ⟨Ca-O⟩ by 0.006 and 0.002 Å, respectively. Hence, this $F^- \leftrightharpoons O^{2-}$ substitution can have an effect on mean bond lengths similar to or even greater in magnitude than those of the more commonly considered cation substitutions. Nevertheless, the changes in mean bond length are not commensurate with the observed variations in cell dimensions. The situation with respect to $OH \leftrightharpoons O^{2-}$ substitution is less clear, as the infrared spectra show that the presence of H in the structure is strongly (but not completely) related to the amount of radiation damage, and most of it probably does not substitute as OH^- for O^{2-} at the O(1) site in the undamaged part of the structure. In addition, $^{[3]}OH$ has a radius similar to that of $^{[3]}O$ (1.34 vs. 1.36 Å) and, therefore, will not have a major effect on polyhedral size considering the probable minor importance of this substitution in the undamaged structure.

The conclusion from this rather involved set of arguments is that for the samples examined here, the variation in cell volume is related to radiation damage effects and is not primarily due to compositional variations. As shown quantitatively for zircon by Murakami et al. (1986), intensity maxima in the powder diffraction patterns of radiation-damaged material are shifted to higher 2θ values because of decreased Bragg diffraction intensities and increased diffuse scattering. These shifts can produce an

TABLE 13. Comparison of electron microprobe analyses by energy dispersive (EDS) and wavelength dispersive (WDS) methods for two partially metamict titanite samples

	Cardiff		M28173	
	EDS	WDS	EDS	WDS
Na_2O	—	0.08	0.12	0.06
CaO	26.97	26.78	26.52	26.04
MgO	0.08	0.12	—	—
MnO	—	0.11	—	0.12
Al_2O_3	3.63	3.63	2.17	1.87
Fe_2O_3	3.59	3.57	3.67	3.66
Y_2O_3	0.70	0.90	1.47	2.02
La_2O_3	—	0.10	—	—
Ce_2O_3	—	0.57	—	0.37
Nd_2O_3	0.21	0.39	—	0.19
SiO_2	29.52	29.92	29.48	29.68
TiO_2	29.77	29.54	31.26	31.32
ZrO_2	0.16	0.16	—	0.03
SnO_2	—	—	—	0.27
Nb_2O_5	0.35	0.42	1.52	1.59
Ta_2O_5	—	—	—	0.29
F	—	2.68	—	1.21
−O = F	—	−1.13	—	−0.51
Sum	94.98	97.84	96.21	98.21
H_2O	—	<1.00	—	<1.00
Total	94.98	<98.84	96.21	<99.21

apparent decrease in cell dimensions. The magnitude of this effect may be assessed by comparing cell dimensions calculated from the positions of the aggregate reflections with those calculated from the positions of the resolved Bragg reflections; the difference for the strongly metamict zircon of Murakami et al. (1986) is ~1% for the cell volume. The difference in cell volumes for the natural and annealed Cardiff titanite samples is ~3%, suggesting that this effect can contribute significantly to cell-volume changes with increasing radiation damage and giving rise to an apparent reduction in the observed cell-volume expansion. From these observations and arguments, we conclude that (1) there is physical expansion of the titanite structure upon metamictization; (2) it is this physical expansion that causes the increase in the unit cell dimensions; and (3) this expansion may be obscured by increased diffuse scattering in the diffraction pattern. This could be further explored by examining titanite with known α-decay doses in the same fashion as Murakami et al. (1986) examined zircon.

Grinding damage

As briefly indicated above, there seems to be a significant difference in the degree of crystallinity for the Cardiff sample, as estimated from its powder diffraction pattern (Fig. 5) and X-ray precession photographs (Fig. 7). The powder diffraction pattern shows very little Bragg diffraction, whereas the precession photographs show prominent (albeit broadened) Bragg diffraction maxima. Precession photographs characterize the original sample, whereas for powder diffraction, the sample must be ground to a grain size of a few micrometers. Such grinding can damage the structure and reduce its crystallinity. From a comparison of the X-ray powder patterns and precession photographs of the four titanite samples examined in detail here, the more radiation-damaged samples seem to have much more grinding damage than the less radiation-damaged titanite samples. Thus the more radiation-damaged samples seem to be more susceptible to grinding damage than nonradiation-damaged crystals, a conclusion that is intuitively reasonable, considering that the structural damage accompanying α-decay must adversely affect the physical properties of the crystal (e.g., Chakoumakos et al., 1988). This being the case, it is important to recognize this effect when assessing the degree of radiation damage using X-ray powder diffraction patterns.

Electron microprobe analyses

Higgins and Ribbe (1976) noted that the weight percent total of the electron microprobe analysis of metamict titanite was low (~95 wt%); this value increased to ~98 wt% on heating. Fleet and Henderson (1985) noted the same feature for an electron microprobe analysis of titanite from Cardiff, Ontario. Our initial electron microprobe work was done by quantitative EDS (energy dispersive spectrometry) analysis on a MAC 5 instrument; the analytical oxide totals showed a negative correlation with the degree of structural damage as estimated from the powder diffraction patterns (Table 1). The analyses were repeated by WDS (wavelength dispersive spectrometry) analysis on a JEOL 733 instrument (see the experimental section). The analyses of the two most damaged samples are compared in Table 13. For the major elements, the analyses are (statistically) identical; no differences exceed two pooled standard deviations. However, the more sensitive WDS method (and the newer instrument) detected the significant amount of F present and gave a much higher REE content, such that the oxide totals for the WDS analyses are 2–3 wt% greater than those of the EDS analyses. However, the total of ~98 wt% is still low. Initially we expected that the difference of 2 wt% might be made up of H_2O, as older wet-chemical analyses of some titanite samples have H_2O up to 2 wt%. Our TG-EGA results show that even in the most radiation-damaged titanite, the evolved (H_2O + H_2) implies that the H_2O content is below 1 wt%. It is notable that, for the Cardiff sample, the total weight loss on heating is in excess of 2 wt% but consists predominantly of SiF_4; possibly the older analyses represent LOI (loss on ignition) as H_2O. Thus, there is not sufficient H_2O to bring the totals of Table 13 up to ~100 wt%, and this deficiency is real, although less than we had originally estimated.

In this regard, it is of interest that our analyses of heated titanite have weight percent totals not significantly different from the analysis totals of the unheated material. This contrasts with the findings of Higgins and Ribbe (1976) and Fleet and Henderson (1985), who recorded significantly higher analysis totals for heated titanite than for unheated radiation-damaged titanite. We further examined this question by reanalyzing the Cardiff titanite sample of Fleet and Henderson (1985). Analyses for unheated and heated material are given in Table 14. The

totals are lower than those obtained for the more Fe-rich Cardiff titanite reported in Table 2, but there is no difference between the analysis totals for the unheated and heated material.

Table 14. Electron microprobe analyses of the Cardiff titanite crystals of Fleet and Henderson (1985)

	Natural*	Heated**	Heated†
CaO	27.87	27.67	27.57
MgO	0.36	0.37	0.35
MnO	0.02	0.02	0.02
Al_2O_3	6.11	6.68	6.21
Fe_2O_3	0.66	0.64	0.64
Y_2O_3	1.05	1.11	1.06
La_2O_3	0.17	0.22	0.17
Ce_2O_3	0.00	0.00	0.00
Nd_2O_3	0.42	0.48	0.42
SiO_2	30.22	30.34	30.21
TiO_2	28.22	27.64	27.90
F	2.55	2.76	2.56
$-O = F$	−1.07	−1.16	−1.08
Sum	96.58	96.77	96.03

* Average of 10 points.
** Annealed in air at 1000 °C for 24 h, average of 10 points.
† Annealed in reducing conditions (Fe/FeO) at 1000 °C for 24 h, average of 11 points.

The metamictization process

Lumpkin and Ewing (1988) have documented the increase in α-decay damage in crystalline pyrochlore structure types, identifying six stages in the metamictization process. The evolution of damage in titanite follows a similar pattern, particularly with respect to the HRTEM observations. The most crystalline sample (M28658) has essentially no damage at all, showing continuous lattice fringes. Sample M28173 shows mottled diffraction contrast caused by strain fields and Frenkel defects around isolated α-recoil and α-particle tracks, corresponding to stage 2 of the Lumpkin-Ewing sequence. The most radiation-damaged sample (Cardiff) shows two types of microstructure. In some areas, there is distinctly mottled diffraction contrast from coexisting crystalline and aperiodic domains produced by overlapping α-recoil tracks, corresponding to stage 4 of the Lumpkin-Ewing sequence. In other areas, there are small, randomly oriented crystallites in a matrix of aperiodic material, the diffraction patterns exhibiting diffuse and spotty diffraction rings. These latter regions may have been initially more damaged than the other areas, but the randomly oriented nature of the crystallites suggests low-temperature annealing. In addition, electron microprobe analyses of Cardiff titanite show some regions of significantly different chemistry, with lower amounts of foreign components, suggesting low-temperature alteration.

Irrespective of the details concerning the fitting and peak assignments in the Mössbauer spectra of the titanite samples examined here, it is clear that nonmetamict titanite (at least that so far examined, including Fe-doped synthetic samples; Holenyi and Annersten, 1987) contains only Fe^{3+}, whereas radiation-damaged titanite (i.e., Cardiff) contains both Fe^{3+} and Fe^{2+}. This suggests that the Fe^{3+} is reduced during the radiation-decay process. The α-decay process of an actinide (A) may be written in the following way:

$$^{A}_{Z}A^{n+} \rightarrow {}^{A-4}_{Z-2}A^{(n-2)+} + {}^{4}_{2}He^{2+}.$$

Normally the oxidation state of the recoil nucleus is rapidly rearranged such that the valence of the parent isotope is preserved in the daughter product (Fielding and White, 1987). However, this process could be complicated by the presence of adjacent transition metals that can easily participate in a more complex reaction by accepting one electron (or even more) during the decay process. In the present case, the Cardiff sample contains significant Fe, all of which was (presumably) in the trivalent state upon initial crystallization. The proposed radioactive decay-reduction process resulted in the formation of significant Fe^{2+}. The Mössbauer parameters are compatible with octahedral coordination of the Fe^{2+}, but the results from the nonmetamict samples indicate that Fe^{2+} is not a significant component of the titanite structure. Consequently, Fe^{2+} most probably occurs in the damaged regions of the structure, which is again compatible with the idea that the reduction of Fe from the trivalent to the divalent state is a feature of the decay process.

It seems reasonable to conclude from the analytical and IR results that high H_2O levels in titanite are associated with α-decay damaged materials. As undamaged titanite has far lower levels of H_2O, this suggests that H had been introduced into the damaged part of the titanite sample, either during or subsequent to damage formation. The H ion is small and very mobile and can diffuse easily and rapidly through a structure. Indeed, the ubiquity of H in most nominally anhydrous minerals indicates that this is the norm rather than the exception. The presence of a large number of radiation-induced defects associated with α-decay damage, together with the presence of H diffusing through the structure (both damaged and undamaged) suggest that H and defects react to produce an OH group. This would account for the occurrence of OH primarily in the aperiodic material. Another relevant feature is the wide range of OH environments indicated by the polarized single-crystal IR spectra of α-decay damaged titanite. For periodic materials, OH-stretching bands are usually quite sharp, and any significant local disorder is expressed as fine structure in the principal stretching band. OH formation by H reaction with radiation-induced defects seems likely to produce OH in an extremely wide range of environments, in accord with the observed IR spectra.

From the X-ray diffraction data, it is apparent that the unit cell volume increases during metamictization and that this expansion is reversible on heating. What is the physical basis of this expansion? If we assume that the radiation damage process is (more or less) isochemical, then the undamaged structure will not change, and the damaged (aperiodic) regions will not contribute to the diffraction; if this were actually the case, then the diffraction results would show no evidence of structural expan-

sion. There are two ways in which this situation may not hold:

1. If the damaged regions are small, then only a few bonds are broken, and the surrounding structure essentially constrains the atoms (close to) their ideal positions, except for some relaxation due to the damage itself; this is the case for damage with a high surface-to-volume ratio, as is true for single α-recoil and α-particle tracks. The scattering from these damaged parts of the structure would still be coherent with the scattering from the undamaged parts of the structure, and the local relaxation would lead to an observed expansion of the long-range structure.

2. If the damaged regions are large, then many bonds are broken, and there are large volumes of aperiodic material; scattering from these regions does not contribute significantly to the observed diffraction maxima (except at extreme degrees of metamictization). Within this aperiodic material are islands of crystalline material (Fig. 16) that will each give coherent Bragg diffraction. However, these crystalline regions have a large surface area, and consequently a significant proportion of the remaining crystalline material shows relaxation due to interface effects. The large expansion of the unit cell in such material (e.g., Cardiff) suggests that this interface relaxation involves an expansion of the structure in this region.

If this model is correct, one would expect a gradual increase in strain through stage 1 of the Lumpkin-Ewing sequence, as relaxation is partially constrained by the surrounding crystalline structure. In stage 2, the damaged regions are no longer constrained by a structurally coherent matrix, and one would expect less strain. This is consistent with the strain estimates in crystalline to metamict pyrochlore measured by X-ray diffraction line broadening (Lumpkin and Ewing, 1988).

With increasing radiation damage, the isotropic displacement parameters of all atoms in the titanite structure increase significantly. As found by Fleet and Henderson (1985), all the titanite samples show anisotropic behavior, with enhanced displacement along **c** ($U^{33} \gg U_{11}, U_{22}$) indicative of disorder in this direction; this is more marked for Ca than for Ti. However, all anisotropic displacement parameters increase with increasing radiation damage, suggesting increased positional disorder with increasing metamictization. This is also in line with the increase in intensity of the +5 eV pre-edge feature in the Ti*K* edge XANES, going from sample M28658 to the Cardiff sample, which signifies increasing disorder around the Ti site.

The structure of metamict titanite

Three principal models have been proposed for the structure of metamict materials: (1) retention of short-range crystalline order (Ringwood, 1985), (2) phase decomposition to a microcrystalline arrangement of related structure types (Graham and Thornber, 1974), and (3) formation of an aperiodic random network structure (Ewing, 1975). Lumpkin and Ewing (1988) have evaluated these three models for metamict minerals of the pyrochlore group and have concluded that model 3 is the most consistent with X-ray diffraction, HRTEM, and EXAFS-XANES measurements.

Aperiodic regions in the HRTEM images of the Cardiff titanite sample (Fig. 16) display patterns of random contrast consistent with the random network model for the metamict state. Although a detailed quantitative interpretation of the images is not feasible because of sample thickness effects, there is no evidence to support the microcrystalline models of the metamict state. The SAED pattern for the Cardiff titanite sample shows a diffuse scattering band with an equivalent *d*-value of 3.0 Å. As discussed by Lumpkin and Ewing (1988), this may be converted to an equivalent interatomic separation by multiplying this value by 1.2, resulting in a mean interatomic spacing of 3.6 Å. The ⟨M-M⟩ (next-nearest-neighbor) separation in the crystalline phase, weighted for differences in scattering efficiency, is ~3.5 Å. This similarity suggests that the prominent diffuse scattering band in the SAED pattern of the Cardiff titanite corresponds to the mean next-nearest-neighbor separation in the random network structure of the metamict material, with the next-nearest-neighbor separation expanded slightly (~3%) over that found in the crystalline phase. The increase in intensity of the Ti*K* edge XANES pre-edge feature at +5 eV is indicative of increasing departure from local centrosymmetry around the Ti site going from crystalline to partially metamict to glassy titanite. This could be due either to increased positional disorder around the Ti site or to a change in coordination number for at least part of the Ti. In the XANES of the titanite glass sample, the +45 eV feature indicates the presence of $^{[4]}$Ti. The EXAFS results indicate that the ratio of $^{[4]}$Ti to $^{[6]}$Ti is 0.09:0.91. There is a slight shoulder in the XANES spectrum of the Cardiff titanite sample at +45 eV that may indicate the presence of $^{[4]}$Ti. However, comparison with the analogous feature in the titanite glass sample indicates that a much smaller proportion of Ti is four-coordinate in the Cardiff sample. As only 0.09 Ti pfu is four-coordinate in the titanite glass sample, we must conclude that the amount of $^{[4]}$Ti in the aperiodic regions of the Cardiff titanite sample is not significant (i.e., $\ll$1% relative) with respect to the structure of the aperiodic material.

The XANES and Fourier transforms of the EXAFS show that there are only small differences in the structures of the crystalline and α-decay damaged titanite samples. This contrasts with the spectra of structures in which the Ti-containing octahedra are joined by sharing edges or even faces [e.g., aeschynite-(Y), euxenite]. The latter structures apparently suffer much greater structural rearrangement during the metamictization process, an intuitively reasonable conclusion. In addition, the XANES spectra for both crystalline and metamict titanite are similar to those of metamict members of the pyrochlore group (Greegor et al., 1984), again suggesting a similar aperiodic network structure.

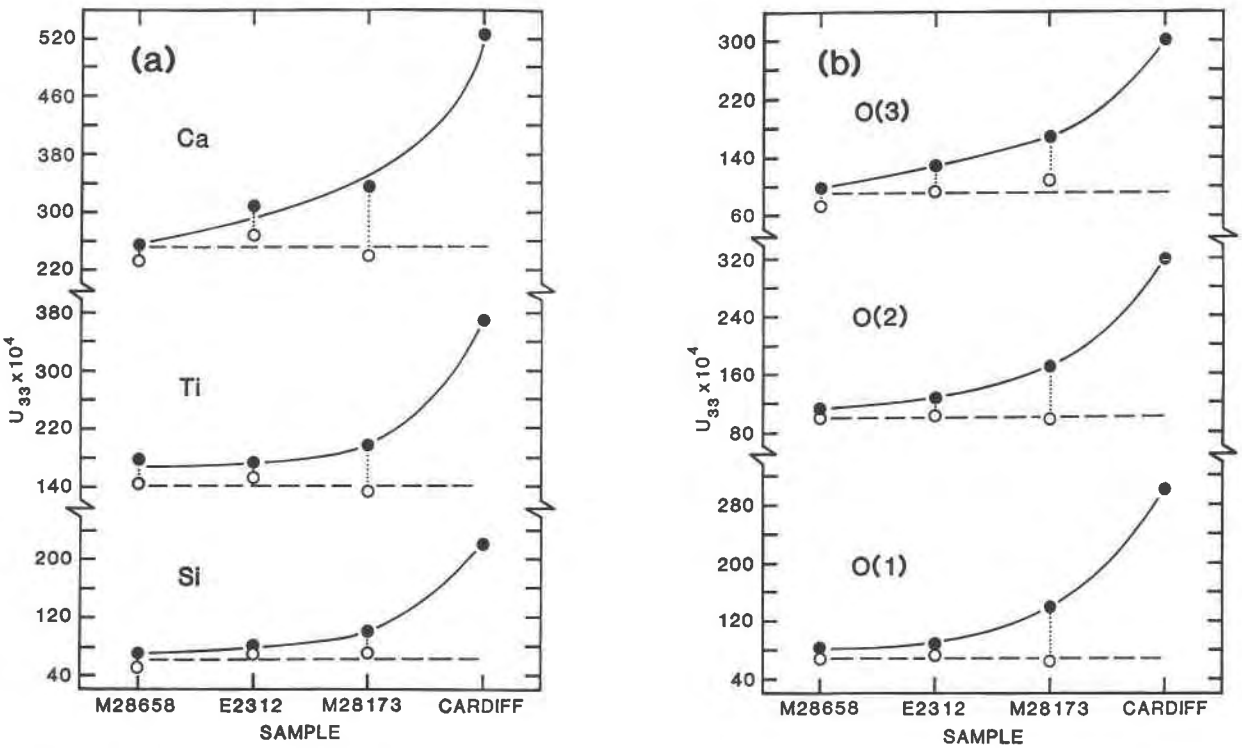

Fig. 20. U_{33} values for cations and anions in natural and heated titanite samples. The values for the three least metamict samples reduce to a common set of values on heating.

High-temperature annealing

Comparison of powder diffraction patterns for natural and annealed Cardiff titanite show that the crystallinity of α-decay damaged titanite is significantly enhanced by heating. This result is further borne out by the crystal structure refinement results on partly metamict and annealed titanite (Table 7; see also Fleet and Henderson, 1985).

However, the single-crystal data provide additional information on this process, particularly through the anisotropic displacement parameters derived from the refinements. Figure 20 shows a graphical representation of the behavior of these parameters on heating of the four titanite samples. As is apparent from Table 7, U_{33} is (usually by far) the largest component of the displacement for each atom, and there is a consistent increase in the magnitude of this parameter with increasing degree of metamictization. High-temperature annealing for the first three titanite samples (M28658, E2312, and M28173) gives rise to reduction in the magnitude of U_{33} to approximately the same value for each cation and anion (Fig. 20); the U_{33} values for cations are still significantly higher than those of U_{11} and U_{22}, indicating that the incipient domain structure is still present in the annealed material. The reduction of the U_{33} values for these three samples to the same set of values suggests that the structural damage has been (more or less) completely annealed and that the original completely crystalline structure has been restored. In contrast to this, the U_{33} values for annealed Cardiff titanite are not reduced to the same set of common values as those of the other three structures. This suggests that the structure of Cardiff titanite has not been completely restored to its original crystalline state. The reduction in U_{33} values does indicate some recrystallization, but it is obviously not complete; of course this is not apparent from the powder diffraction data of the annealed material, as such data are less sensitive to such subtle structural detail.

The infrared spectra are also instructive in this regard. Comparison of the powder spectra of metamict and annealed Cardiff titanite (Fig. 10) shows that the spectral detail in the crystalline titanite spectrum (Fig. 9) is not totally restored by high-temperature annealing. This was surprising, since infrared spectroscopy is a short-range technique as compared to X-ray diffraction. However, this result is consistent with results of the structure refinements showing that the structure of Cardiff titanite is not completely restored upon high-temperature annealing. Together, these results collectively suggest that high-temperature annealed Cardiff titanite consists of regions of highly crystalline titanite and regions of aperiodic structure (from which many of the defects have been re-

moved by annealing). Both the crystalline and noncrystalline regions contribute to the observed IR spectrum of the annealed material, and thus there is a significant broadened spectral component from the aperiodic material, resulting in a spectrum that is not as sharp as that from nonmetamict crystalline titanite. This cannot totally explain the infrared spectra. It is also significant that the very prominent band at $\sim 670\ cm^{-1}$ (observed in the most highly crystalline titanite) is not restored upon heating, even though the sharper bands at lower energies are restored (Fig. 10). Presumably this band is related to long-range periodicity that is rapidly destroyed with small amounts of radiation damage, and this periodicity is not restored by annealing when significant amounts of radiation damage have accumulated.

The high-temperature annealing sequence suggested here is in line with the degree and type of structural damage observed in HRTEM images of the different samples. At low degrees of damage, α-recoil tracks and small islands of aperiodic material are observed in a matrix of crystalline titanite. At this stage, annealing will restore the initial crystalline structure because the amount of atomic movement required for this process is small and well constrained by the surrounding structure. As the amount of aperiodic material increases, the memory effect imposed by the continuous matrix of crystalline titanite is gradually lost as this matrix becomes discontinuous. In the case of Cardiff titanite, there are approximately equal volumes of crystalline and aperiodic material. Where the aperiodic regions are locally small and well constrained by surrounding crystalline titanite, there is recrystallization; for other regions in which this is not the case, the aperiodic regions are annealed to form a fairly stable aperiodic structure free of defects, the latter being suggested by the restoration of thermoluminescence sensitivity upon annealing (Khalifa and Durrani, 1986).

An unexpected feature of the TG-EGA results was the identity of the principal species involved in particular temperature ranges. In the intermediate temperature range (500–1000 °C), one group of samples evolved significant quantities of H_2, and the other group evolved primarily H_2O. In some minerals (e.g., amphiboles, micas), the thermal evolution of H_2 is related to a local auto-oxidation and dehydroxylation reaction involving Fe^{2+} and OH. This is not the case here, as sample E2312 has no significant Fe^{2+} and yet evolved significant H_2 in the intermediate temperature range. This behavior is also not correlated with the degree of α-decay damage, as sample E2335 (damage index of 8) evolved primarily H_2O, whereas the Cardiff sample (damage index of 10) evolved primarily H_2. Significant H_2 is evolved only when a significant amount of F is present, whereas H_2O is the predominant species when F is absent. It is difficult to avoid the conclusion that the presence of F in titanite is a major factor controlling the character of the evolved volatiles at lower temperatures.

It is also notable that at high temperature, F-rich titanite evolves significant amounts of SiF_4, whereas low-F titanite does not evolve any such complex species. We have no mechanism to suggest as an explanation for these results but note that (in hindsight) we have seen the same effect in other silicate minerals; it seems that this phenomenon is unconnected with α-decay damage. A more specific investigation of this effect in minerals is underway.

Low-temperature annealing

The HRTEM images of the Cardiff material show two areas of structure, one corresponding to stage 4 of the Lumpkin-Ewing metamictization sequence, and the other showing randomly oriented crystallites in a matrix of aperiodic material. The latter structure does not correspond to one of the normal stages in the metamictization process, suggesting that this structure has been influenced by some other process in addition to radiation damage. A notable characteristic of these areas is the random orientation of the crystalline islands, which suggests that these regions have been significantly perturbed by this second process.

Contrast between two compositional types of structure is seen in backscattered electron images obtained using the electron microprobe (Fig. 21 left). Predominantly along fractures, there are areas of titanite with a composition significantly different from the other areas of the crystals. The association of these areas with fractures suggests that they have been subject to (postmetamictization) alteration by low-temperature solutions. As well as causing alteration, this would also cause low-temperature recrystallization of the aperiodic parts of the titanite sample, the physical changes associated with this alteration causing a (more or less) random reorientation of the remaining crystalline islands. The compositional effects of this process are apparent in Table 2. The low-temperature solutions have partly leached these regions of nonessential titanite constituents; thus, Ca and Ti increase and REE, Fe, and F are reduced. Figure 21 (right) shows a similar backscattered electron image for the experimentally annealed Cardiff titanite sample. Again there is the significant compositional difference associated with prominent primary fractures, but also apparent is very extensive fracturing throughout the crystal, a feature that must be a result of the high-temperature annealing process.

Let us consider the mechanism by which this low-temperature process proceeds, focusing primarily on the aperiodic regions of the structure. The normal metamict material has the same composition as the original titanite sample (except perhaps for the valence state of Fe), and its structure consists of a corner-sharing heteropolyhedral network. With $^{[3]}O$, the local bond-valence requirements of the O atoms are well satisfied for $^{[4]}Si$, $^{[6]}Ti$, and $^{[6]}Ca$ or $^{[7]}Ca$. Substitution of Fe^{2+} or REE for Ti or Ca in this type of structure perturbs this structure, disrupting the local bond-valence distribution. It seems more reasonable that these constituents be incorporated into the network associated with Frenkel defects. This being the case,

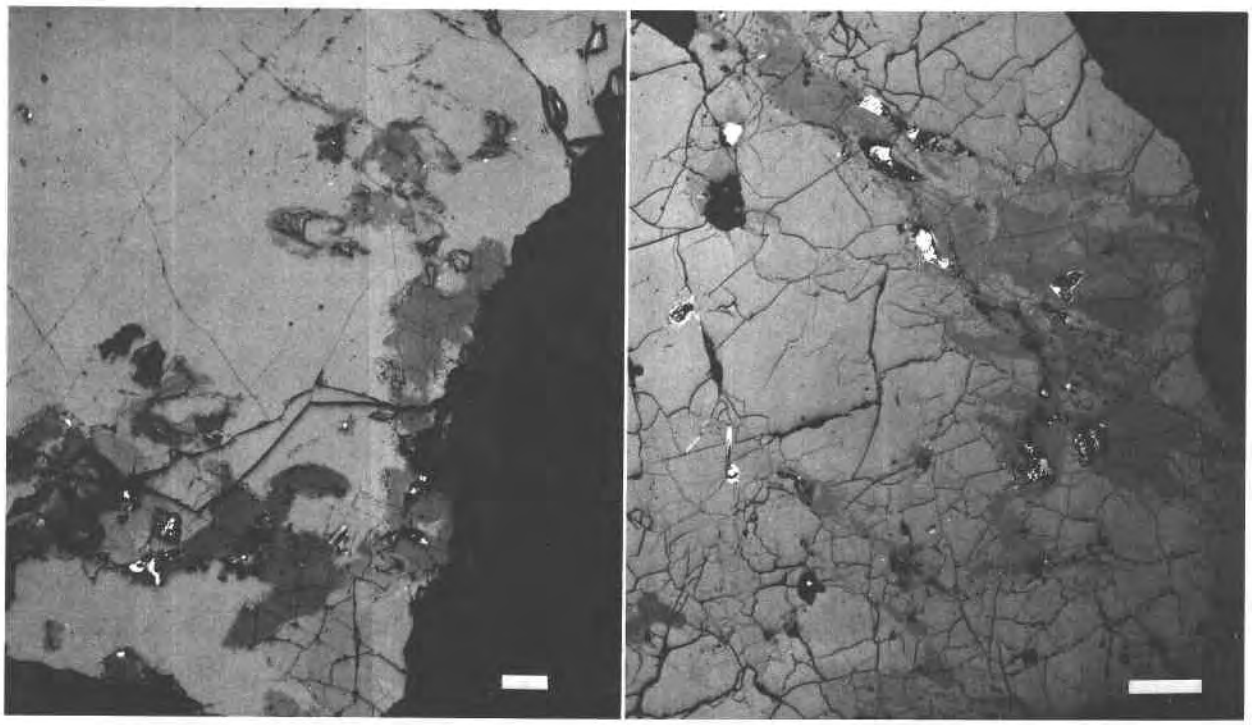

Fig. 21. Backscattered electron images of unheated (**left**) and heated (**right**) Cardiff titanite, showing the compositional contrast between the normal stage 4 metamict areas and the altered areas associated with primary fractures in the crystal. There is extensive cracking in the heated titanite. Scale bars are 100 μm.

such components would be more susceptible to leaching than components that are held in the framework itself; this may account for the enhanced removal of Fe (as Fe^{2+}?) and REE relative to Al^{3+} and Zr^{4+}, which are more likely to be incorporated into the aperiodic structure as framework constituents. Thus in the annealed material, the low-temperature annealing may selectively destroy accumulated Frenkel defects while leaving the more extended α-decay damage. This may be relevant to leaching mechanisms in α-decay damaged nuclear waste forms.

Acknowledgments

This work was supported by the Natural Sciences and Engineering Research Council of Canada in the form of operating grants to F.C.H., F.J.W., and M.E.F.; an infrastructure grant to F.C.H.; major equipment grants to F.C.H. and F.J.W.; university research fellowships to F.C.H. and C.M.; a postdoctoral fellowship to B.L.S.; and a postgraduate scholarship to L.A.G. The Department of Energy, Office of Basic Energy Sciences, supported R.C.E. and G.R.L. (grant DE-FG04-84ER45099). The National Science Foundation supported the work of G.R.R. (grant EAR-8618200). The manuscript was substantially improved by reviews from François Farges and Alex Speer, and by the editorial pen of Glenn Waychunas.

References cited

Aines, R.D., and Rossman, G.R. (1986) Relationships between radiation damage and trace water in zircon, quartz and topaz. American Mineralogist, 71, 1186–1193.

Bair, R.A., and Goddard, W.A. (1980) Ab initio studies of the X-ray absorption edge in copper complexes. 1. Atomic Cu^{2+} and $Cu(II)Cl_2$. Physical Review B, 2767–2776.

Bancroft, G.M., Metson, J.B., and Kresovic, R.A. (1987) Leaching studies of natural and synthetic titanites using secondary-ion mass spectrometry. Geochimica et Cosmochimica Acta, 51, 911–918.

Beran, A. (1970) Messung des Ultrarot-Pleochroismus von Mineralen. IX. Der Pleochroismus der OH-Streckfrequenz in Titanit. Tschermaks Mineralogische und petrographische Mitteilungen, 14, 1–5.

Chakoumakos, B.C., Murakami, T., Lumpkin, G.R., and Ewing, R.C. (1987) Alpha-decay-induced fracturing in zircon: The transition from the crystalline to the metamict state. Science, 236, 1556–1559.

Chakoumakos, B.C., Oliver, X.Y., and Ewing, R.C. (1988) Mechanical property measurements on damaged zirconia. Eos, 69, 475.

Dollase, W.A. (1975) Statistical limitations of Mössbauer spectral fitting. American Mineralogist, 60, 257–264.

Ewing, R.C. (1975) The crystal chemistry of complex niobium and tantalum oxides. IV. The metamict state: Discussion. American Mineralogist, 60, 728–733.

Ewing, R.C., Chakoumakos, B.C., Lumpkin, G.R., and Murakami, T. (1987) The metamict state. Materials Research Society Bulletin, 58–66.

Fielding, P.E., and White, T.J. (1987) Crystal chemical incorporation of high-level waste forms in aluminotitanate-based ceramics: Valence, location, radiation damage, and hydrothermal stability. Journal of Materials Research, 2, 387–394.

Fleet, M.E., and Henderson, G.S. (1985) Radiation damage in natural titanite by crystal structure analysis. Materials Research Society Symposium Proceedings, 50, 363–370.

Fyfe, C.A., Gobbi, G.C., Hartman, J.S., Lenkinski, R.E., O'Brien, J.H., Beange, E.R., and Smith, M.A.R. (1982) High-resolution solid-state MAS spectra of ^{29}Si, ^{27}Al, ^{11}B and other nuclei in organic systems using a narrow bore 400 MHz high-resolution nmr spectrometer. Journal of Magnetic Resonance, 47, 168–173.

Graham, J., and Thornber, M.R. (1974) The crystal chemistry of complex niobium and tantalum oxides. IV. The metamict state. American Mineralogist, 59, 1047–1050.

Greegor, R.B., Lytle, F.W., Sandstrom, D.R., Wong, J., and Schultz, P. (1983) Investigation of TiO_2-SiO_2 glasses by X-ray absorption spectroscopy. Journal of Noncrystalline Solids, 55, 27–42.

Greegor, R.B., Lytle, F.W., Ewing, R.C., and Haaker, R.F. (1984) Ti-site geometry in metamict, annealed and synthetic complex Ti-Nb-Ta oxides by x-ray absorption spectroscopy. Nuclear and Instrumental Methods, Physical Research B1, 587–594.

Groat, L.A., Hawthorne, F.C., Carter, R.T., and Ercit, T.S. (1985) Tantalian niobian titanite from the Irgon Claim, Southeast Manitoba. Canadian Mineralogist, 23, 569–571.

Groat, L.A., Raudsepp, M., Hawthorne, F.C., Ercit, T.S., Sherriff, B.L., and Hartman, J.S. (1990) The amblygonite-montebrasite series: Characterization by single-crystal structure refinement, infrared spectroscopy, and multinuclear MAS-NMR spectroscopy. American Mineralogist, 75, 992–1008.

Grunes, L.A. (1982) A study of core excitation spectra in 3d transition metals and oxides by electron energy loss spectroscopy and X-ray absorption spectroscopy. Ph.D. thesis, Cornell University, Ithaca, New York.

Hawthorne, F.C., Groat, L.A., Raudsepp, M., and Ercit, T.S. (1987) Kieserite, a titanite-group mineral. Neues Jahrbuch für Mineralogie Abheilungen, 157, 121–132.

Hayward, P.J. (1988) Glass ceramics. In W. Lutze and R.C. Ewing, Eds., Radioactive waste forms for the future, p. 427–492. Elsevier, New York.

Hayward, P.J., and Cecchetto, E.V. (1981) Development of sphene-based glass ceramics tailored for Canadian waste disposal conditions. In S.N. Topp, Ed., Scientific basis for nuclear waste management, vol. IV, p. 91–98. Elsevier, New York.

Higgins, J.B., and Ribbe, P.H. (1976) The crystal chemistry and space groups of natural and synthetic titanites. American Mineralogist, 61, 878–888.

Holenyi, Katalin, and Annersten, Hans (1987) Iron in titanite: A Mössbauer-spectroscopic study. Canadian Mineralogist, 25, 429–433.

Hollabaugh, C.L., and Foit, F.F., Jr. (1984) The crystal structure of an Al-rich titanite from Grisons, Switzerland. American Mineralogist, 69, 725–732.

Hollabaugh, C.L., and Rosenburg, P.E. (1983) Substitution of Ti for Si in titanite and new end-member cell dimensions for titanite. American Mineralogist, 68, 177–180.

Howard, C.J., and Sabine, T.M. (1964) X-ray diffraction profiles from neutron-irradiated magnesium oxide. Journal of Physics C, 7, 3453–3466.

International Tables for X-Ray Crystallography, Vol. III (1974) The Kynoch Press, Birmingham, England.

Khalifa, M.S., and Durrani, S.A. (1986) Fission tracks and thermoluminescence (TL) properties of natural sphene crystals. International Journal of Radiation, Applications and Instrumentation Part D, Nuclear Tracks and Radiation Measurements, 12, 867–870.

Lumpkin, G.R., and Ewing, R.C. (1988) Alpha-decay damage in minerals of the pyrochlore group. Physics and Chemistry of Minerals, 16, 2–20.

Lutze, W., and Ewing, R.C. (1988) Summary and evaluation of nuclear waste forms. In W. Lutze and R.C. Ewing, Eds., Radioactive waste forms for the future, p. 699–740. Elsevier, New York.

Lytle, F.W., Greegor, R.B., Sandstrom, D.R., Marques, E.C., Wong, J., Spiro, C.L., Huffman, G.P., and Huggins, F.E. (1984) Measurement of soft X-ray absorption spectra with a fluorescent ion chamber detector. Nuclear Instruments and Methods, 226, 542–548.

McMillan, P.F., and Hofmeister, A.M. (1988) Infrared and Raman spectroscopy. In Mineralogical Society of America Reviews in Mineralogy, 18, 99–159.

Mongiorgi, R., and Riva de Sanseverino, L. (1968) A reconsideration of the structure of titanite, $CaTiOSiO_4$. Mineralogica et Petrographica Acta, 14, 123–141.

Muir, I.J., Metson, J.B., and Bancroft, G.M. (1984) ^{57}Fe Mössbauer spectra of perovskite and titanite. Canadian Mineralogist, 22, 689–694.

Murakami, Takashi, Chakoumakos, B.C., and Ewing, R.C. (1986) X-ray powder diffraction analysis of alpha-event radiation damage in zircon ($ZrSiO_4$). Advances in Ceramics, 20, 745–753.

Paul, B.J., Cerny, Petr, Chapman, Ron, and Hinthorne, J.R. (1981) Niobian titanite from the Huron Claim pegmatite, southeastern Manitoba. Canadian Mineralogist, 19, 549–552.

Ringwood, A.E. (1985) Disposal of high-level nuclear wastes: A geological perspective. Mineralogical Magazine, 49, 159–176.

Robbins, C.R. (1968) Synthetic $CaTiOSiO_4$ and its germanium analogue ($CaTiOGeO_4$). Materials Research Bulletin, 3, 693–698.

Sandstrom, D.R., Lytle, F.W., We, P.S.P., Greegor, R.B., Wong, Joe, and Schultz, Peter (1980) Coordination of Ti in TiO_2-SiO_2 glass by X-ray absorption spectroscopy. Journal of Non-Crystalline Solids, 41, 201–207.

Sherriff, B.L. (1984) An investigation of the application of ^{29}Si magic angle spinning nuclear magnetic resonance in geology. M.Sc. thesis, Brock University, St. Catharines, Ontario.

Speer, J.A., and Gibbs, G.V. (1976) The crystal structure of synthetic titanite, $CaTiOSiO_4$, and the domain texture of natural titanites. American Mineralogist, 61, 238–247.

Stern, E.A., and Heald, S.M. (1979) X-ray filter assembly for fluorescence measurements of x-ray absorption fine structure. Reviews of Scientific Instruments, 50, 1579–1582.

Stout, P.J., Lumpkin, G.R., Ewing, R.C., and Eyal, Y. (1987) An annealing study of alpha-decay damage in natural UO_2 and ThO_2. Materials Research Society, Proceedings, 112.

Taylor, Mark, and Brown, G.E., Jr. (1976) High-temperature structural study of the $P2_1/a = A2/a$ phase transition in synthetic titanite, $CaTiOSiO_4$. American Mineralogist, 61, 435–447.

Vance, E.R., and Metson, J.B. (1985) Radiation damage in natural titanites. Physics and Chemistry of Minerals, 12, 255–260.

Waychunas, G.A. (1987) Synchrotron radiation XANES spectroscopy of Ti in minerals: Effects of Ti bonding distances, Ti valence, and site geometry on absorption edge structure. American Mineralogist, 72, 89–101.

Zachariasen, W.H. (1930) The crystal structure of titanite. Zeitschrift für Kristallographie, 73, 7–16.

Manuscript received October 23, 1989
Manuscript accepted January 13, 1991